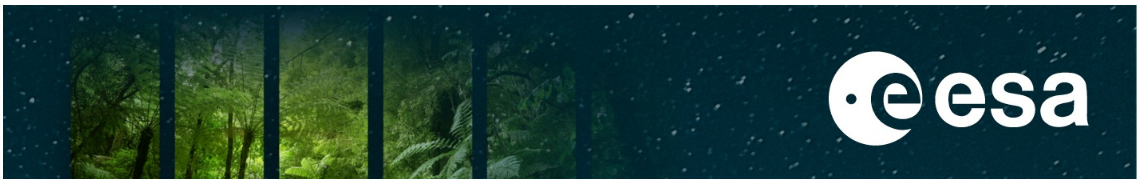

ESA Living Planet Fellowship
Final Report

HI-FIVE: High-Resolution Forest Coverage with InSAR & Deforestation Surveillance

Author:
Dr. Ing. Francescopaolo Sica

Host institution:
Microwaves and Radar Institute
German Aerospace Center (DLR)
Münchener Str. 20, 82234 Weßling, Germany

January 2022

Table of Contents

List of Figures

List of Tables

List of Abbreviations

AA Average Accuracy metric

AASR Azimuth Ambiguity to Signal Ratio

ALOS Advanced Land Observing Satellite-1

CLC CORINE Land Cover (map)

CORINE CooRdination of INformation on the Environment

DL Deep Learning

DLR Deutsches Zentrum für Luft- und Raumfahrt

DTAR Distributed Target Ambiguity Ratio

ESA European Space Agency

ESD Enhanced Spectral Diversity

FDBAQ Flexible Dynamic Block Adaptive Quantization

FROM-GLC Finer Resolution Observation and Monitoring of Global Land Cover

GLCM Gray Level Co-Occurrence Matrix

HI-FIVE High-Resolution Forest Coverage with InSAR & Deforestation Surveillance

InSAR Interferometric SAR

IW Interferometric Wide swath (mode)

LC Land Cover

LUT Look-Up-Table

ML Machine Learning

NDMI Normalized Difference Moisture Index

NDVI Normalized Difference Vegetation Index

OA Overall Accuracy metric

PALSAR Phased Array type L-band SAR

PNOTS Programa Nacional de Observación de la Tierra por Satélite

PRODES Programa de Calculo do Desflorestamento da Amazonia

RASR Range Ambiguity to Signal Ratio

RF Random Forests

RGB Red-Green-Blue channel

RMSE Root-Mean-Square-Error

S-1 Sentinel-1 system

S-2 Sentinel-2 system

S-3 Sentinel-3 system

SADH Sum And Difference Histograms

SAR Synthetic Aperture Radar

SCL Scene CLassification

SLC Single Look Complex

SNR Signal-to-Noise Ratio

SWIR Short-Wave-InfraRed channel

TAXI experimental TanDEM-X Interferometric processor

TDM TanDEM-X Mission

TDX TanDEM-X

TOPS Terrain Observation with Progressive Scans

TSX TerraSAR-X

WP Working Package

1. Executive summary

Inferring land cover from space has a central role in the Remote Sensing field, and its popularity has increased dramatically in the last few years. Latest advances in spaceborne systems allow for the continuous coverage of the Earth's surface at periodical intervals and on a global scale, enabling systematic monitoring of the land-use dynamics. An excellent example is the Copernicus Programme coordinated by the European Commission in partnership with the European Space Agency (ESA), which provides thousands of acquisitions per year all around the globe, covering almost all the electromagnetic spectrum with five dedicated families of Sentinel satellites. Among them, the Sentinel-1 (S-1) mission is the first free data provider of Synthetic Aperture Radar (SAR) imagery worldwide and constitutes an unprecedented monitoring system able to detect a large variety of natural phenomena.

Within the framework of the HI-FIVE project - High-Resolution Forest Coverage with InSAR & Deforestation Surveillance - awarded through the ESA's Living Planet Fellowship program, I investigated novel Machine Learning-based methodologies to timely monitor the world's forests from Sentinel-1 interferometric SAR data. In particular, I focused on how to exploit best the peculiarity of the Sentinel-1 system, such as:

- precise acquisition geometry
- fixed revisit time and broad coverage
- interferometric capabilities

The significant contribution of this project has been to provide scientific evidence about interferometric coherence being a crucial parameter to classify land cover from SAR data accurately. Additionally, different frameworks have been proposed to exploit Sentinel-1 time series. The provided algorithms have been successfully applied to map forest coverage in Europe and Brazil, specifically over the Amazon rainforest. My investigations have proved the ability of coherence time series to accurately follow forest coverage changes and therefore track deforestation phenomena promptly, down to a monthly timescale resolution. I further developed Deep Learning approaches to increase the temporal and spatial resolution. Specifically, the Φ-Net has been proposed to estimate the interferometric coherence accurately at the highest possible resolution, i.e., close to Sentinel-1 Single Look Complex (SLC) original resolution. Similarly, the temporal resolution has been targeted. An image segmentation algorithm based on the U-Net architecture has been developed to improve classification performance and to set the groundwork for single image land cover classification, which allows in the future for change detection down to a monthly scale. The performed work aims to represent a reference for future research work, which can benefit from the findings coming from this project.

The present manuscript provides an overview of the HI-FIVE project, from its main objectives and work-plan to the main findings and recommendations for future research investigations. Section 2 is dedicated to the description of project objectives and the original schedule. Section 3 shows all the performed research investigation and its results. Specifically, state-of-the-art algorithms are presented in Section 3.1, the description of the developed methodologies is provided in Section 3.2 The exploited data sets are reported in Section 3.3 and the obtained results in Section 3.4. Eventually, in Section 4 I summarize the main findings of the project and give recommendations for future research investigations. Additionally, I provide the scientific outcome of the project in terms of published journal and conference papers in Section 5.

2. Objectives and work-plan

Forests are vital for the Earth's ecosystem since they reduce the concentration of carbon dioxide in the atmosphere and control climate changes. Studying deforestation, global forest coverage, and biomass development are fundamental for assessing their impact on the ecosystem. Remote sensing represents a powerful tool for constant monitoring at a global scale of vegetated areas. In particular, given the daylight independence and the capability to penetrate clouds, spaceborne SAR systems represent a unique solution for mapping and monitoring forests. Sentinel-1, with its broad coverage and short revisit time [1], is a breakthrough technology, ideal for the generation of a constantly updated forest coverage map product and the rapid monitoring of large-scale areas, aiming at detecting ongoing deforestation activities and forest disturbance. Even though the detected SAR backscatter already provides valuable forest coverage and structure information, SAR interferometry (InSAR) adds valuable and reliable information to the classification method. In particular, the temporal dynamic of the interferometric coherence, with a sampling period of 6 or 12 days, is investigated and modeled for different types of land cover. The accurate estimation of InSAR and backscatter parameters is of fundamental importance for approaching this analysis. The use of interferometric is vital to shorten the observation time and provide a time-tagged accurate forest classification.

The HI-FIVE research project aims to investigate the potential of Sentinel-1 InSAR data for the semantic segmentation of the land cover and its dynamic with time. The main objective has been to develop advanced image processing methods and implement strategies for generating high-resolution maps of forest coverage and deforestation from Sentinel-1 InSAR data. In particular, with my research project, I aimed to develop methodologies based on Earth Observation platforms and Machine Learning (ML) tools for global and systematic observation of the world's forests and the accurate measurement of the amount of ongoing deforestation and its temporal evolution. The project specifically targeted the monitoring of forested areas, but a general framework for land cover classification has been proposed. Indeed, all the presented methodologies can be easily generalized to multiple and more complex classification tasks.

The project proposal has been framed to provide novel and efficient algorithms for forest mapping with Sentinel-1 data stacks. In the specific, the systematic acquisition with a 6 or 12 days time interval has been an object of analysis. I focused on optimizing the approach to detect changes in terms of resolution in space (high-resolution maps) and time (quick response to deforestation activities). The derived features from both multi-temporal backscatter and interferometry are used as input for different ML-based approaches for land cover classification, starting from the Random Forests algorithm to more advanced models, such as Deep Learning ones.

The analysis has been supported with additional experiments at the X band to support the finding at the C band with Sentinel-1 and further investigate the effect of a large perpendicular baseline on the estimation of temporal interferometric parameters. Indeed, since both temporal and volume decorrelation phenomena affect the coherence measurement in repeat-pass systems, the use of repeat-pass coherence may be detrimental, especially in areas with diverse vegetation cover. For this analysis, I use X band data from the German bistatic TanDEM-X constellation [2] combined with the Spanish twin satellite, PAZ [3]. This investigation further provides a practical framework for comparing and using data from different sensors, which could be applied in the design of future missions.

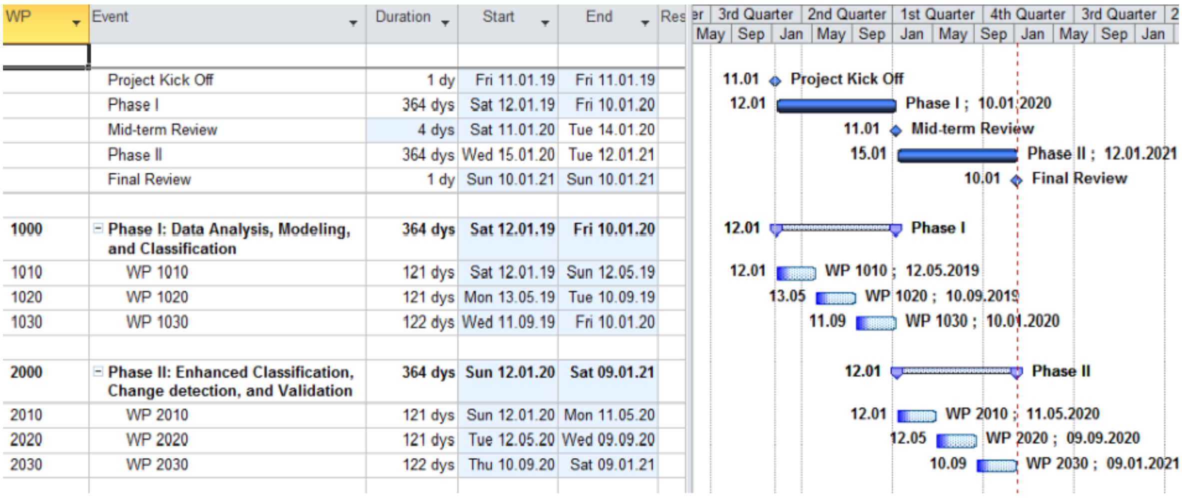

Figure 1: HI-FIVE overall work-plan.

The project has been organized on a two-year schedule and organized in two phases as depicted in Figure 1.

Phase I has been dedicated to creating the Sentinel-1 interferometric processing chain. It included the processing to obtain coherence stacks, the estimation of the temporal decorrelation, and the actual ML-based classification algorithm. I focused on the general classification framework during this phase and tested it over Europe. Furthermore, I applied the classifier to map forest coverage and tested it over the Amazon rainforest. The single tasks as proposed initially are depicted in the block diagram of Figure 2.

Phase I includes three main work packages:

- WP1010: implementation of the algorithms necessary to the InSAR and backscatter parameters estimation
- WP1020: data analysis and modeling from Sentinel-1 and TanDEM-X data
- WP1030: classification based on machine learning classifiers

The Parameters Estimation block, in WP1010, implements several types of estimations:

- Nonlocal estimation for stack as proposed in [4]
- Moving average filtering with a selection of different windows shapes and dimensions
- Texture measures as proposed in [5]
- Estimation of temporal and spatial statistics
- Geocoding of the derived quantities to a common posting

All the estimated parameters are related to a given acquisition geometry.

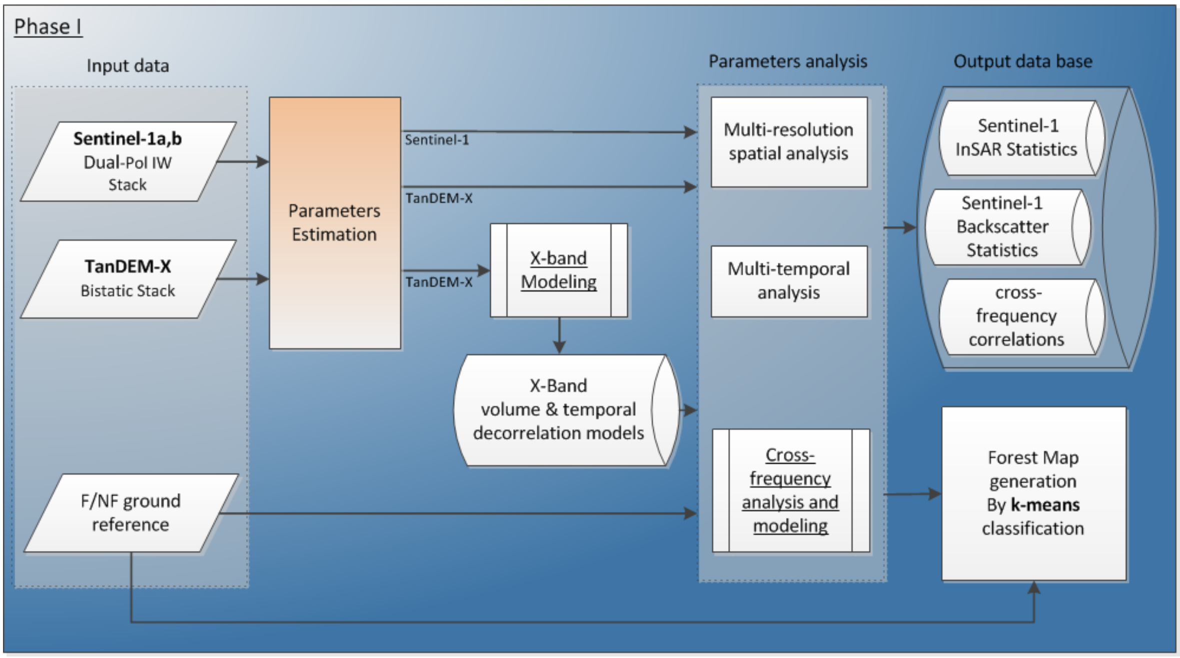

Figure 2: Block scheme for phase I.

Given the obtained findings in the course of the project, the research investigation has had slight modifications, such as using DL methodologies to estimate the interferometric parameters. Indeed, the proposed Φ-Net approach [6] has been shown better estimation performance and execution time when compared to the nonlocal filters proposed initially.

Phase II has been dedicated to investigating change detection strategies and DL approaches to improve classification accuracy. Furthermore, I investigated decorrelation phenomena at the X band by exploiting the synergy between the TanDEM-X and PAZ constellations. In this way, I exploited time series with a minimum revisit time of 4 days and computed temporal decorrelation coefficients for several land cover classes.

The block diagram, including all the tasks for this phase, is depicted in Figure 3 and Figure 4 shows the operations computed in the parameter estimation block.

Phase II is organized in the following work packages:

- WP2010: classification using Deep Learning algorithms
- WP2020: implementation of change detection strategies and fusion of Sentinel-1 and Sentinel-2 (S-2) multi-spectral data
- WP2030: validate the classification result using external reference data

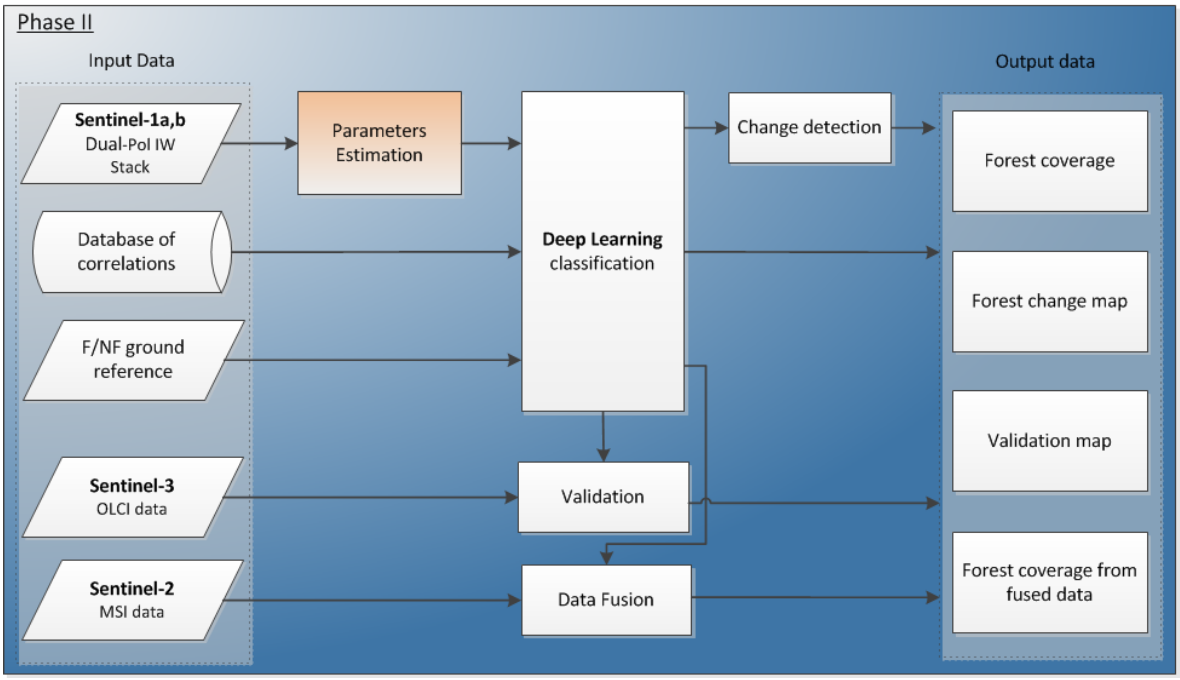

Figure 3: Block scheme for phase II.

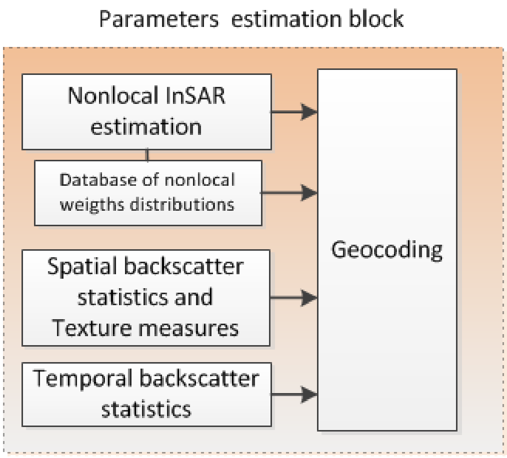

Figure 4: Block scheme for parameter estimation block.

3. Work performed

3.1 Scientific context

In the last decades, the effective monitoring of forests has been addressed with a large variety of RS approaches. Different research investigations focused on forest mapping and tackling the detection of possible degradation caused by either natural events or human activities, such as selective logging or illegal deforestation.

Optical and laser sensors have been largely applied for mapping forests extent and its changes [7], [8], [9]. At the same time, the determination of forests biomass has been further addressed [10] [11] as well as land cover mapping [9]. Given the extended cloud coverage that can hide large areas from optical sensors during most of the year, spaceborne radar sensors, capable of acquiring data independently on weather and daylight conditions, represent a necessary tool for constant monitoring at a global scale. For this purpose, detected SAR backscatter is widely exploited for land cover characterization and specifically forest mapping [12], [13], [14]. The analysis of backscatter signature indeed has led to the development of successful techniques and the release of operational products. An example is the global forest/non-forest map from L-band ALOS PALSAR data, which was generated by properly thresholding backscatter levels in the cross-polarization channel HV [15]. Furthermore, to retrieve aboveground biomass indicators, backscatter statistics and texture have been analyzed for tropical rainforests in [16] and for boreal forests in [17]. More recently, the joint use of data at different operative bands has been investigated as well, showing encouraging results [18].

The advantage of exploiting coherence information over forested areas was firstly investigated in [19]. Alternatively, single-pass interferometry has been exploited by using the TanDEM-X bistatic coherence. Specifically, the volume decorrelation component has been computed and used to generate the global TanDEM-X Forest/Non-Forest Map [20] [21]. The combined use of interferometric coherence and backscatter has shown promising results, as shown in [22], where Cosmo-SkyMED data was considered. More extensive studies on multi-temporal data were carried out at C band, using ERS-1/2 data acquired during the tandem mission phase, for forested areas [23], for wheat fileds [24], and for general land cover classification [25] [26] [27] [28] [29]. Accordingly, the first automatic classification strategies based on machine-learning classifiers exploit long time series with an observation interval that varies from several months up to years and classify the target on the base of its backscatter temporal dynamic and coherence parameters [30],[31].

More recently, the large availability of repeat-pass data with exact orbit definition has allowed for the reliable use of SAR interferometry (InSAR) for many different applications, such as deformation and natural hazards monitoring or topography reconstruction. In this framework, the Sentinel-1 mission opened new avenues for land cover classification using time series data. It comprises two satellites (S-1A and S-1B), which allow for a short revisit time of 12 or 6 days if one single or both satellites are employed. It operates at the C band and acquires large swaths of about 250 km in range using the Interferometric Wide (IW) swath mode [32]. The advance brought by this system is the fixed revisit time, which allows for modeling temporal parameters that can be linked to land cover classes. It is precisely these criteria that I investigated in this project, as it will be shown in the next section.

3.2 Methods

Unlike state-of-the-art methodologies, the proposed research investigation focuses explicitly on the use of interferometric temporal decorrelation from InSAR time series. The HI-FIVE project focuses on using Sentinel-1 stacks to retrieve land cover information from the temporal dynamic of the SAR amplitude and InSAR coherence parameters. Nevertheless, other sensors, such as the TerraSAR-X/TanDEM-X and PAZ satellites, are also considered a matter of comparison and support the findings. In the following, I will present the main developed methodologies, including the general framework for the land cover classification from Sentinel-1 time series, the approach to forest coverage mapping, and its changes over time. The latter can detect changes down to a monthly scale, allowing for forest protection policies. DL methodologies have been further investigated to improve classification accuracy and spatial and temporal resolution. The Φ-Net, for example, is dedicated to improving the estimation of the coherence maps and their spatial resolution. The classification accuracy is targeted instead by using a U-Net model.

3.2.1 Temporal decorrelation retrieval in InSAR time series

The degree of similarity between two SAR images composing an interferometric pair is measured through the interferometric coherence, i.e., the modulus of their complex correlation. By assuming wide-sense stationarity of all the involved processes, i.e., amplitude, phase, and intensities, the coherence can be estimated as follows [33]:

$$\hat{\rho}[p] = \frac{\left|\sum_{i\in\Omega(p)} x_i y_i^*\right|}{\sqrt{\sum_{i\in\Omega(p)}|x_i|^2 \sum_{i\in\Omega(p)}|y_i|^2}}. \tag{3.1}$$

Note that for Sentinel-1 data, the coherence estimation is performed through a moving average filter. The kernel size is set to 5×19 or 7×27 depending on the desired end-product resolution of 50×50 or 100×100 meters, respectively. I additionally remove the possible bias occurring for low coherence values by applying the equation in [34], which relates coherence, number of looks, and bias.

Given a stack of SLCs of size M and a revisit time T, I generate all the interferograms within a given temporal baseline of $N \cdot T$ days, with $\max(N) = M - 1$. All the available interferograms have hence a temporal baseline given by $\delta t = n \cdot T$ with $n \in [1, N]$. Before the coherence estimation, I apply the common-band filter in azimuth and range [35] to avoid decorrelation due to spectral shift and baseline.

According to [36], the measured coherence ρ_{tot} can be factorized as the product of different components that are ascribed to a single decorrelation phenomenon:

$$\rho_{\text{tot}} = \rho_{\text{temp}}\, \rho_{\text{vol}}\, \rho_{\text{amb}}\, \rho_{\text{az}}\, \rho_{\text{rg}}\, \rho_{\text{quant}}\, \rho_{\text{SNR}}, \tag{3.2}$$

where the different terms stand for the coherence contribution due to (from left to right):

- temporal decorrelation (ρ_{temp})

- volume decorrelation (ρ_{vol})
- SAR ambiguities (ρ_{amb})
- relative shift of the Doppler spectra (ρ_{az})
- baseline decorrelation (ρ_{rg})
- quantization noise (ρ_{quant})
- limited SNR (ρ_{SNR})

As I will show in the following, the first two terms can be ascribed to specific scattering mechanisms if correctly separated from the rest. Therefore it is possible to associate a given decorrelation value to a specific observed target, e.g., the land cover. In this project, I focus on extracting the interferometric temporal decorrelation for land cover purposes.

The Sentinel-1 InSAR constellation

Sentinel-1 is the ESA SAR satellite system developed within the Copernicus Earth Observation program. It comprises two twin SAR satellites, Sentinel-1A (S-1A) and Sentinel-1B (S-1B), operating at C band in single and dual polarization and flying along the same nominal orbit, shifted by 180 degrees. Sentinel-1 combines wide swath imaging at medium resolution with a significant amount of routine daily acquisitions to form a powerful land cover mapping and monitoring instrument. Among the four different acquisition modes, in this work, I considered the products provided in the IW mode, which guarantees a frequent operational interferometric capability (6 days repeat-pass), covering large areas of 250 kilometers swath with 5×20 meters nominal resolution [37].

The decorrelation factors for the Sentinel-1 constellation can be described as follows:

- ρ_{SNR}: once computed the signal-to-noise ratios of the primary SNR_1 and secondary SNR_2 images by considering the derived gamma naught from the different images and the corresponding annotated noise profiles [38], the factor associated to the limited signal-to-noise ratio equals [39]:

$$\hat{\rho}_{\text{SNR}} = \frac{1}{\sqrt{(1+\text{SNR}_1^{-1})(1+\text{SNR}_2^{-1})}}, \tag{3.3}$$

- ρ_{quant}: the used FDBAQ quantization scheme adapts the number of quantization bits to the local backscatter level to minimize the signal-to-quantization noise ratio [40]. Given the high performance of the algorithm, a contribution close to 1 is considered.

- ρ_{amb}: the coherence loss corresponding to SAR ambiguities can be approximated by [39]:

$$\rho_{\text{amb}} = \frac{1}{(1+\text{AASR})}\frac{1}{(1+\text{RASR})}, \tag{3.4}$$

where AASR and RASR are the azimuth and range ambiguity to signal ratios, respectively. For Sentinel-1 I refer to the quantities $\mathrm{az}-\mathrm{DTAR}$ and $\mathrm{rg}-\mathrm{DTAR}$ presented in [41]. The worst case shows $\mathrm{az}-\mathrm{DTAR} = -25.29$ dB (IW1 subswath) and $\mathrm{rg}-\mathrm{DTAR} = -26.10$ dB (IW3 subswath) for the IW mode. This values, when applied to eq.(3.4), lead to $\rho_{\mathrm{amb}} = 0.99$, which is therefore neglected.

- ρ_{az} and ρ_{rg}: these two decorrelation factors are automatically compensated when applying common-band azimuth and range filter during the generation of the interferogram.
- ρ_{vol}: given Sentinel-1 small orbital tube of only 50 m radius [32], the volume decorrelation factor can be neglected [42]. This assumption is also sustained by experimental observations from the analysis of X band bistatic TanDEM-X data in [43], where it was observed that, for such small baselines, no significant decorrelation is detected.

Therefore, the Sentinel-1 interferometric system is by nature suitable for the separation between volume and temporal decorrelation $\hat{\rho}_{\mathrm{temp}}$. The latter is therefore obtained by performing the simple ratio:

$$\hat{\rho}_{\mathrm{temp}} = \frac{\hat{\rho}}{\hat{\rho}_{\mathrm{SNR}}}. \tag{3.5}$$

Note that values of coherence $\hat{\rho}$ that lay within the bias level cannot be corrected, and therefore the corresponding pixels are associated to the maximum possible decorrelation.

The TanDEM-X/PAZ InSAR constellation

TerraSAR-X (TSX) and TanDEM-X (TDX) are two Earth observation SAR satellites belonging to the same constellation, launched in 2007 and 2010, respectively, within a public-private partnership, between the German Aerospace Center (DLR) and Airbus Defence and Space. This bistatic interferometric system can perform high-resolution single-pass interferometric acquisitions with a maximum resolution of 1 meter. Both spacecraft fly in a close formation with flexible interferometric baseline selection, building a highly re-configurable constellation [39]. In February 2018, a third satellite was added to this constellation: the Spanish PAZ. It is an X band SAR mission from the Spanish national Earth observation program (PNOTS) for security and defense needs and is owned and operated by Hisdesat. It is an almost twin version of the TerraSAR-X satellite and flies on the same nominal orbit [3].

The whole constellation constituted by these three satellites allows for the acquisition of dense time series, obtained by combining the monostatic channel of the TanDEM-X constellation (TDM) with PAZ, allowing for a highly flexible constellation with an improved acquisition capability and reduced revisit time. Indeed, the satellites have a revisit time of 11 days and are displaced over the same orbit with a 4 days separation, forming a 4+7 days constellation. As an example, Figure 5 shows all possible interferometric pairs with corresponding temporal baselines for a TDM-PAZ time series composed by 5 acquisitions.

The TDM-PAZ constellation presents both large spatial and temporal baselines. After the compensation of system-dependent decorrelations as already explained for the Sentinel-1 system, the coherence results in the following η parameter:

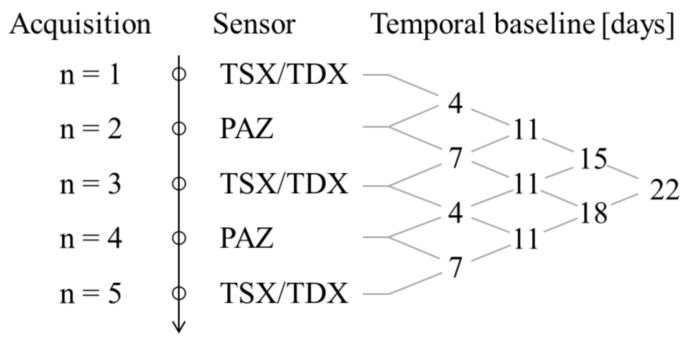

Figure 5: Acquisition timeline of the TDM-PAZ constellation showing the available temporal baselines.

$$\eta = \rho_{\text{vol}}\rho_{\text{temp}} \tag{3.6}$$

Therefore, the correct retrieval of the temporal decorrelation is subject to a prior estimation of the volume decorrelation. This correction is done in two steps. First, the volume decorrelation is computed for a specific class. Second, it is compensated to the η parameter. This procedure is suitable only for analyzing a known observed land cover class and not for classification purposes. The implementation details for this technique can be found in [44].

The first step towards the separation of volume and temporal decorrelation consists of retrieving the amount of volume decorrelation ρ_{vol} at different spatial baselines and for each considered land cover class. For this purpose, I exploit TanDEM-X bistatic acquisitions, which are characterized by the absence of temporal decorrelation ($\rho_{\text{temp}} = 1$) and isolate the ρ_{vol} factor by compensating for all other decorrelation sources, as done in [43]. Afterward, I compute the mean ρ_{vol} per image and fit the dependency of such volume decorrelation factors with respect to the height of ambiguity h_{amb} with an exponential function:

$$\rho_{\text{vol}}(h_{\text{amb}}) = 1 - \alpha e^{-\frac{h_{\text{amb}}}{\beta}}. \tag{3.7}$$

The estimated parameters $\hat{\alpha}$ and $\hat{\beta}$ are the optimal ones in the least-square sense. Once ρ_{vol} is correctly modeled from bistatic data, it can be used to compensate the η factor in eq.(3.2.1) and isolate the temporal contribution. In this way, I can accurately retrieve the temporal decorrelation factor ρ_{temp} at a given temporal baseline δt. Finally one can fit $\rho_{\text{temp}}(\delta t)$ for the considered land cover class by iterating this process for each of the multi-temporal interferometric pairs and then fitting the exponential model in [45].

3.2.2 Framework for land cover classification from Sentinel-1 time series

As the first step for the classification of the land cover, I focused on three fundamental aspects:

1. Processing of Sentinel-1 data
2. Modeling of the temporal decorrelation in Sentinel-1 time series
3. Analysis of the correlation between interferometric parameters and land cover classes

In the following, I recap the main aspects of the proposed methodology and remand to the full paper in [46] for details. The proposed methodology considers the combined use of SAR backscatter and interferometric parameters. The block diagram in Figure 6 shows the implemented processing chain. For simplicity and when not strictly necessary, only one index indicates bi-dimensional image coordinates.

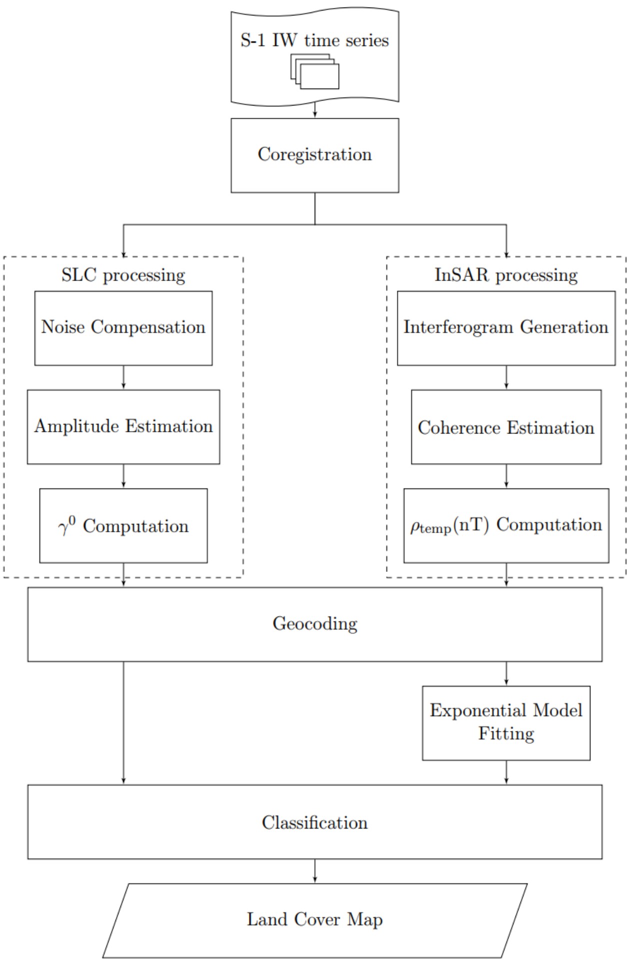

Figure 6: Sentinel-1 processing chain. Left branch: backscatter processing. Right branch: interferometric processing.

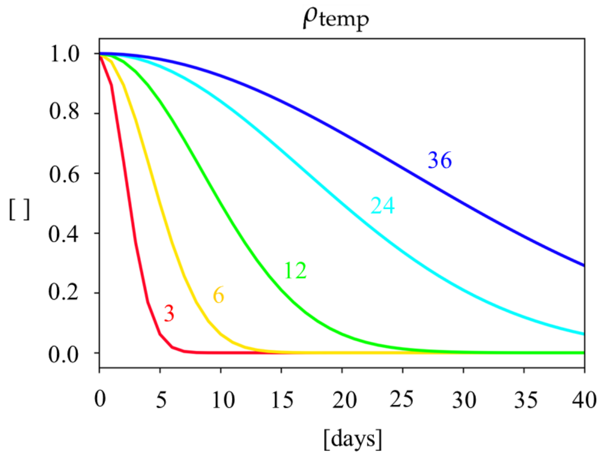

Figure 7: Exponential model of ρ_{temp} as in eq.(3.8), derived for $\rho_{\text{LT}} = 0$ and different values of τ (from 3 to 36 days).

Temporal decorrelation model

The temporal decorrelation in InSAR time series is often modeled as a decaying exponential. Motivated by experimental evidence [45], [47], in this work, I modeled the C band InSAR decorrelation of Sentinel-1 time series as an exponential decaying according to the square of the time, with unitary starting value at time zero.

The model of the evolution in time of the temporal decorrelation factor $\rho_{\text{temp}}(\delta t)$ is set to:

$$\rho_{\text{temp}}(\delta t) = (1 - \rho_{\text{LT}})\, e^{-\left(\frac{\delta t}{\tau}\right)^2} + \rho_{\text{LT}}, \tag{3.8}$$

with τ the target decorrelation factor and ρ_{LT} the long-term coherence. The latter term considers that some targets may not completely decorrelate even after a long time and that low coherence values present a considerable estimation bias. Figure 7 shows the behavior of such a model for different values of τ and assuming $\rho_{\text{LT}} = 0$.

As it can be observed from eq.(3.8), ρ_{temp} equals 1 for $\delta t = 0$ and tends to ρ_{LT} for $\delta t \to \infty$, while its decay velocity is regulated by the target decorrelation constant: a lower τ means a faster decay and viceversa. After a time interval τ, the exponential function decreases from a value of 1 to $1/e$ (where e is the Neper constant). The sampling of the temporal decorrelation factor model is $\delta t = nT$, where T represents the satellite revisit time and $n \in [0, \infty[$.

Sentinel-1 interferometric processing chain

In the following, I describe the processing needed to obtain the required interferometric parameters from Sentinel-1 stacks starting from the focused SAR data. Given a stack of M focused Sentinel-1 IW mode acquisitions, these need first to be coregistered with respect to a common primary geometry. The latter is chosen as the one closest to the central acquisition date of the entire stack. The coregistration of each S-1 TOPS data has been done accurately following the processing steps described in [48] by exploiting DLR's interferometric processor

TAXI [49]. After a preliminary geometrical coregistration, the enhanced spectral diversity (ESD) technique is applied to the overlapping areas between subsequent bursts. This procedure allows for achieving an azimuth coregistration accuracy in the order of thousands of the azimuth pixel size.

Following the block diagram of Figure 6, after the coregistration of the entire stack, the main branch is split into two sub-processing chains: the *SLC processing*, for the estimation of the multi-temporal backscatter γ^0, and the *InSAR processing*, for the estimation of the temporal decorrelation factor. In this case, the retrieved ρ_{temp} is then projected over a 100×100 meters geocoded grid, which matches with the resolution of the external reference map. Eventually, the exponential fitting is performed along the time dimension to retrieve the τ and ρ_{LT} parameters.

SLC processing

Land classification applications require an almost exclusive dependence of backscatter on the physical properties of the observed target [50], [51]. For this purpose, I apply radiometric correction to the Sentinel-1 digital number and compute the gamma-naught coefficient γ^0. Furthermore, the system noise floor is removed using the designated Look-Up-Table (LUT) provided within Sentinel-1 data to retrieve a single value for the time series. The amplitude is eventually estimated A_m for the m^{th} SLC ($m \in [0, M[$) by assuming local spatial stationarity and applying a 7×27 pixels moving average filter:

$$\hat{A}_m[p] = \sqrt{\sum_{i \in \Omega(p)} {A_m}^2[i]}, \tag{3.9}$$

where p is the current estimated pixel, and $\Omega(p)$ a 7×27 boxcar window around p.

Hence the γ^0 is computed using the local incidence angle θ_{inc} and the calibration factor K as:

$$\hat{\gamma}^0_m = K\hat{A}_m \tan\left(\theta_{\text{inc}}\right), \tag{3.10}$$

where $\hat{\gamma}^0_m$ represents the derived γ^0 for the m^{th} image within the stack. Eventually, to obtain a single gamma-naught for the whole stack, all the computed $\hat{\gamma}^0$ are averaged together as:

$$\hat{\gamma}^0 = \sum_{m=1}^{M} \hat{\gamma}^0_m. \tag{3.11}$$

InSAR processing

Given the stack of M SLCs, all the interferograms within a given temporal baseline of $N \cdot T$ days are generated, with $\max(N) = M - 1$. All the available interferograms have hence a temporal baseline given by $\delta t = n \cdot T$ with $n \in [1, N]$. Before the coherence estimation, the common-band filter in azimuth and range [35] is applied to avoid decorrelation due to spectral shift and baseline. For the sake of clarity, I indicate with the i-subscript the $i - th$ pixel of the image. Assuming now the local stationarity of the interferometric signal, I estimate the coherence with a 7×27 pixels moving average as:

$$\hat{\rho}[p] = \frac{|\sum_{i\in\Omega(p)} x_i y_i^*|}{\sqrt{\sum_{i\in\Omega(p)}|x_i|^2 \sum_{i\in\Omega(p)}|y_i|^2}}. \tag{3.12}$$

Using the relation between coherence, the number of looks and bias [34], I further compensate for the bias within the coherence estimation. The temporal decorrelation factor ρ_{temp} is therefore isolated from the interferometric coherence by inverting eq.(3.2). As formerly shown, for Sentinel-1 data this corresponds to eq.(3.5).

Exponential model fitting

At this stage, the complete set of temporal decorrelation factors for the entire stack is computed and mapped to a 100×100 meters geo-referenced grid. I exploit all the available interferometric pairs by setting $N = N_{\text{MAX}} = 5$. Therefore the maximal temporal baseline will result in $N \cdot T = 30$ days. For every pixel on ground p the tensor of all computed temporal decorrelation values $\hat{\rho}_{\text{temp}}[n, i, j]$ is defined, where $n \in [1, N]$ spans the temporal axis, $i \in [1, N - n]$ spans all the available values for a given temporal baseline $n \cdot T$, and $j \in \Omega\,(p)$ spans the spatial axis in a square neighborhood $\Omega\,(p)$ of size L around the current estimated pixel.

Before applying the model fitting, I identify those pixels that lose the monotonic decreasing trend along time and show a boisterous behavior because of decorrelation phenomena and residual coherence noise. To overcome this limitation, for these pixels, I consider a larger spatial neighborhood ($L = 5$), while for all the others, $L = 1$. Subsequently, the model fitting is performed with a least-square approach by numerically solving the following functional:

$$(\hat{\tau}\ ,\ \hat{\rho}_{\text{LT}}) = \underset{\tau\ ,\ \rho_{\text{LT}}}{\arg\min} \left\{ \sum_{n=1}^{N} \sum_{i=1}^{N-n} \sum_{j\in\Omega(p)} \left((1-\rho_{\text{LT}})\, e^{-\left(\frac{nT}{\tau}\right)^2} + \rho_{\text{LT}} - \hat{\rho}_{\text{temp}}[n,i,j] \right)^2 \right\}, \tag{3.13}$$

where $\hat{\tau}$ and $\hat{\rho}_{\text{LT}}$ are the estimated target decorrelation constant and long term coherence, respectively.

Classification approach

All previously computed parameters can be jointly exploited in ML-based classifiers. In this project, I considered the Random Forests (RF) classifier, a robust algorithm that provides high classification accuracy while requiring the setting of few hyperparameters [52]. The RF algorithm is non-parametric, i.e., no assumption has to be made on the mapping function, allowing for high flexibility of the algorithm when generalized to unseen data. In applications related to land cover classification, the use of the RF algorithm is relatively recent and has been proven to be a very effective tool for optical, multi/hyper-spectral, and SAR data [53], [54], [55], [56], [57].

Moreover, I aim to quantify the impact that multi-temporal interferometric parameters have on classification performance. For this purpose, I apply the RF algorithm with different input features:

- *case 1*: $\hat{\gamma^0}$, and θ_{inc},
- *case 2*: $\hat{\tau}$, $\hat{\rho}_{\mathrm{LT}}$, and θ_{inc},
- *case 3*: $\hat{\gamma^0}$, $\hat{\tau}$, $\hat{\rho}_{\mathrm{LT}}$, and θ_{inc}.

The local incidence angle θ_{inc} is a significant feature since it carries information on the SAR acquisition geometry. Indeed, it merges the topography information and the satellite position at the moment of the acquisition. By adding this parameter, the typical backscatter dependency from the side-looking nature of SAR sensors can be correctly taken into account by the RF algorithm. In all cases, given the relatively small number of input features, I let the RF algorithm use them all for each of the created trees. I further use the Gini index [58] to minimize the probability of misclassification and set the number of trees in the forest (i.e. the number of estimators, n_est) as well as the minimum number of samples in a leaf node (i.e. the leaf size, $leaf_{size}$) to 50. These last parameters have been experimentally chosen after a preliminary performance analysis. In this work, I classify $K = 3$ different land cover classes. A more diversified classification with a larger number of classes can also be achieved by exploiting the same proposed framework.

Performance evaluation

The comparison between the results is based on evaluating the average accuracy (AA) and the overall accuracy (OA) for all the test areas, considering all the valid pixels in the image under test. Given K classes, the associated confusion matrix C assumes the following form:

$$C = \begin{bmatrix} c_{1,1} & \cdots & c_{1,j} & \cdots & c_{1,K} \\ \vdots & \ddots & \vdots & & \vdots \\ c_{i,1} & \cdots & c_{i,j} & \cdots & c_{i,K} \\ \vdots & & \vdots & \ddots & \vdots \\ c_{K,1} & \cdots & c_{K,j} & \cdots & c_{K,K} \end{bmatrix}, \tag{3.14}$$

where the elements along the main diagonal, $c_{i,j}$ $(i = j)$, represent the correctly predicted pixels for each class $j = 1, ..., K$, i.e. they are called class accuracy, and the sum of the elements along each column j corresponds to the number of pixels belonging to each class $j = 1, ..., K$. The average accuracy defines the mean of each accuracy per single class, i.e., the sum of class accuracy divided by the number of classes. In contrast, the overall accuracy corresponds to the number of correctly predicted pixels divided by the total number of pixels to predict, i.e., the sum of all elements in C. In particular, the respective formulas associated with the two metrics are:

$$AA = \frac{\sum_{j=1}^{K} c_{j,j}}{K} \tag{3.15}$$

and

$$OA = \frac{\sum_{j=1}^{K} c_{j,j}}{\sum_{i=1}^{K} \sum_{j=1}^{K} c_{i,j}}. \tag{3.16}$$

While the overall accuracy assesses the global performance of the classifier, the average accuracy further accounts for accuracy unbalancing between the different classes.

3.2.3 Forest Mapping

The methodology adopted for the forest mapping exploits the same processing scheme depicted in Section 3.2.2, but adds additional parameters as the textures, derived from the computed backscatter, and increases the output resolution, specifically from 100 meters to 50 meters grid. In the following, I will highlight the main methodological differences with respect to the framework already presented in Section 3.2.2 and refer to the publication in [59] for the complete description of the developed algorithms.

To improve the product resolution, a boxcar filter with a fixed-size window of 5×19 pixels was chosen. Given the Sentinel-1 IW mode along azimuth and ground range, $14\ m \times 3.7\ m$ respectively, the output resolution is an almost square cell of $70\ m \times 70.3\ m$. Furthermore, a window centered on the current estimated pixel is favorable for preserving spatial geometries.

Texture Features

In the proposed framework, I further consider the texture as an additional feature, providing important information about the spatial dependency among neighboring pixels. Among the several methods and techniques based on statistical models, I use the Sum And Difference Histograms (SADH) textures described in [60].

A discrete image can be interpreted as the realization of a bidimensional stationery and ergodic process, which means that each pixel of the image, $u_{x,y}$, can be seen as the observation of a random variable. One of the most used statistical approaches to evaluate this relationship is counting the occurrence of the same pixels inside a defined domain D, after quantizing the original image dynamically using a grey level scale with a fixed number of levels N_g. This assumption allows for the generation of a matrix of $N_g \times N_g$ co-occurrence elements, known in literature as Gray Level Co-occurrence Matrix (GLCM) [61], [62]. One of the main properties of the GLCM is its dependency on the relative position of the pixels in the image, $\delta = (\delta_x, \delta_y)$. Indeed, a spatial configuration of the displacement vector defines a precise direction in the co-occurrence counting; in particular, setting the relative position $\delta = (\delta_x, \delta_y)$, the GLCM elements are the results of a comparison between two random variables:

$$\begin{cases} u_{x,y} \\ u_{x+\delta_x, y+\delta_y} \end{cases} \tag{3.17}$$

A much lighter approach for the extraction of the textures is presented in [61]. It makes use of the SADH method, which suggests the measurement of directional sum and difference matrices associated with the displacement vector $\delta = (\delta_x, \delta_y)$. Each element of such matrices, $s_{x,y}$ and $d_{x,y}$, respectively, is given by:

$$\begin{cases} s_{x,y} = u_{x,y} + u_{x+\delta_x,y+\delta_y} \\ d_{x,y} = u_{x,y} - u_{x+\delta_x,y+\delta_y} \end{cases} \tag{3.18}$$

This strategy facilitates the computation of spatial textures since determining the co-occurrence matrix is no longer needed. Indeed, the second-order joint probability function associated to the $u_{x,y}$ and $u_{x+\delta_x,y+\delta_y}$ can be approximated as the product of the first-order probability functions of the sum and difference defined in (3.18), which, by definition, are uncorrelated random variables [60]. Therefore, the probability density functions $\hat{P}_s(i)$ and $\hat{P}_d(j)$, $(i, j = 1, ..., N_g)$, of sum and difference, is estimated by normalizing the relative histograms for the total number of counts. Using the SADH approach, I extract nine informative textures [61]:

- Average (AVE): describes the mean co-occurrence frequencies
- Cluster prominence (CLP): expresses the tailedness of the image in terms of kurtosis
- Cluster shade (CLS): observes the asymmetry of the image in terms of skewness
- Contrast (CON): corresponds to a statistical image stretching
- Correlation (COR): explains the linear dependency of gray level values
- Energy (ENE): describes the uniformity of a texture
- Entropy (ENT): characterizes the degree of disorder in the image
- Homogeneity (HOM): represents the degree of similarity among gray tones within an image
- Variance (VAR): defines the dispersion of shades of gray around the mean value μ

For the application of this method, I set the domain D to 5×19 pixels and the number of gray levels $N_\mathrm{g} = 20$, to obtain a final output resolution that is consistent with one of the other estimated parameters γ^0, τ, and ρ_LT.

The feature extraction using the SADH method is repeated twice, considering the most significant displacement vectors along both the azimuth $d = (1, 0)$ and the slant-range $d = (0, 1)$ directions. In Figure 8 I named these two set of textures as $SADH_{(1,0)}$ and $SADH_{(0,1)}$, respectively.

Classification approach

After geocoding, all the previously described feature maps are posted to the final resolution of 50×50 meters and serve as input to a RF classifier. As in [46], I considered the Gini index as impurity measurement for the classifier, and I set the number of estimators, i.e., the number of decision trees and the minimum number of samples in a leaf node to 50.

Following the branches of the block diagram in Figure 8, a set of Sentinel-1 time series can be downloaded and processed, deriving a total of 22 feature maps, 18 textures plus the 4 parameters proposed in [46]. Table 1 summarizes the complete set of features considered in this work.

Table 1: List of the 22 features considered. Column $ORIG$ shows the parameters used in Section 3.2.2, while columns $SADH_{(1,0)}$ and $SADH_{(0,1)}$ show the textures extracted along both azimuth $d = (1, 0)$ and slant-range $d = (0, 1)$.

$ORIG$	$SADH_{(1,0)}$	$SADH_{(0,1)}$
$\hat{\gamma^0}$	$AVE_{(1,0)}$	$AVE_{(0,1)}$
$\hat{\tau}$	$CLP_{(1,0)}$	$CLP_{(0,1)}$
$\hat{\rho}_{\mathrm{LT}}$	$CLS_{(1,0)}$	$CLS_{(0,1)}$
θ_{inc}	$CON_{(1,0)}$	$CON_{(0,1)}$
	$COR_{(1,0)}$	$COR_{(0,1)}$
	$ENE_{(1,0)}$	$ENE_{(0,1)}$
	$ENT_{(1,0)}$	$ENT_{(0,1)}$
	$HOM_{(1,0)}$	$HOM_{(0,1)}$
	$VAR_{(1,0)}$	$VAR_{(0,1)}$

The experiments on the RF classifier in two different cases, characterized by a different set of input features:

- case *(ORIG)*: $\hat{\gamma^0}$, $\hat{\tau}$, $\hat{\rho}_{\mathrm{LT}}$, and θ_{inc},
- case *(SADH)*: $\hat{\gamma^0}$, $\hat{\tau}$, $\hat{\rho}_{\mathrm{LT}}$, θ_{inc}, $SADH_{(1,0)}$, and $SADH_{(0,1)}$.

The *(ORIG)* test case is equivalent to the settings used for the land cover classification, which represents my baseline. The *(SADH)* test case instead additionally uses the 18 textures extracted from γ^0 by using the SADH method.

3.2.4 Monthly deforestation monitoring

The presented methodology for forest mapping can be successfully applied for the timely detection of deforestation phenomena. As previously shown, the mapping algorithm can achieve a temporal resolution of a single month. It means that the generated maps could also be used to track coverage changes on a monthly scale. For this application I use the methodology presented in Section 3.2.3 and refer to the paper in [63] for all implementation details. The processing scheme for the generation of the monthly forest maps is depicted in Figure 8.

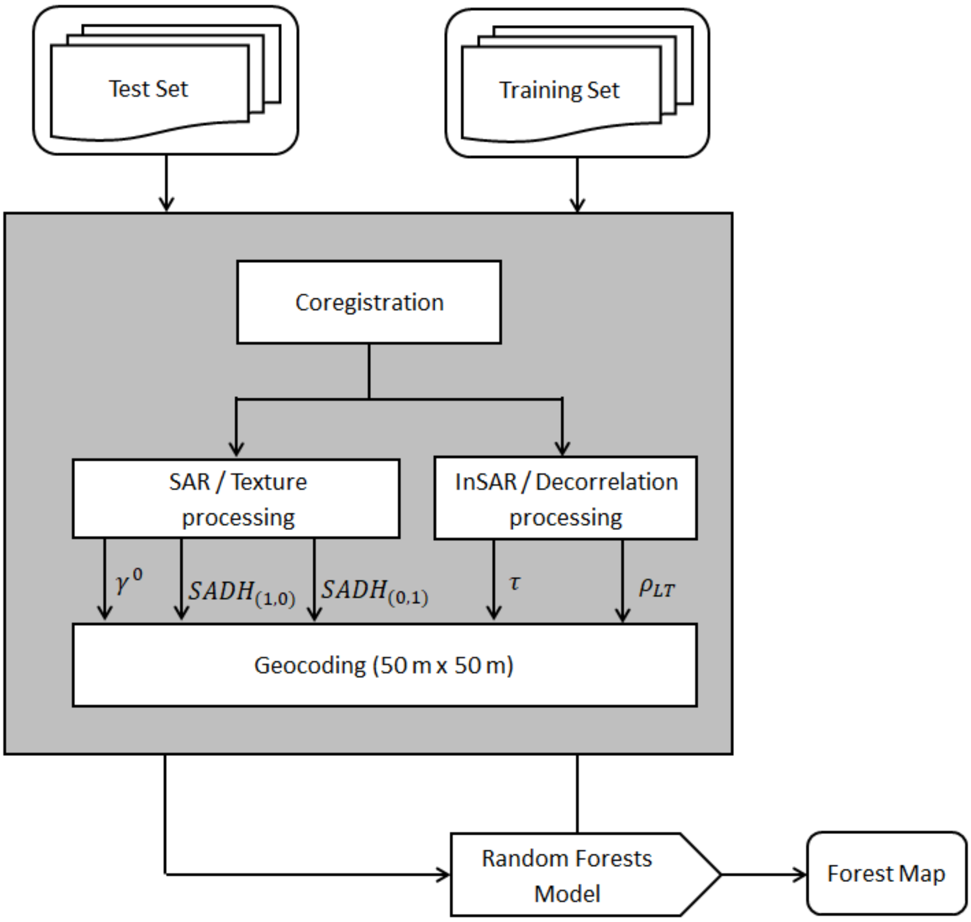

Figure 8: Sentinel-1 processing chain with the integration of Sum and Difference Histograms (SADH) textures proposed.

Change detection may be applied at a variety of different conceptual levels. The simplest form would be to differentiate between subsequent pixel values in time as already done in [64]. In this work, I use a slightly more complex algorithm, which foresees a segmentation procedure before the actual change detection. Specifically, an area is detected as a change if a whole segment is missing and not a single pixel. On the one hand, this strategy guarantees higher accuracy by reducing false positives. On the other hand, the minimum detectable area increases, and minimal changes are not detected.

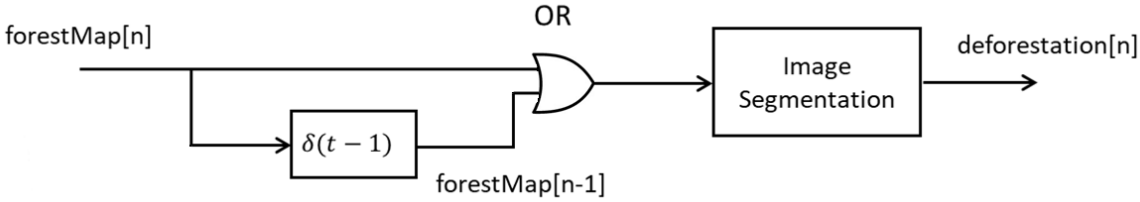

Figure 9: Processing scheme of the automatic change detection strategy for evaluating the deforestation on the n-th month. The block $\delta(t-1)$ represents the 1-month delay that has to be considered for generating the new deforestation map.

The algorithm is summarized in Figure 9. Since it is expected that changes will happen on adjacent pixels, the algorithm aims to detect a whole area by performing pixel clustering. I apply an image segmentation based on morphological watershed transformation [65] that regards the image intensity as a topographic map and is very useful to this purpose.

Using a segmentation algorithm to identify clear-cut polygons has two main advantages. It first identifies groups of pixels likely to be associated with the same physical object on the ground. Moreover, this also allows for a certain tolerance to image misalignments, which might arise from minor image distortions. Using the watershed segmentation, one can guarantee the detection of clear-cuts not smaller than 75 ha.

Performance evaluation

By discarding the invalid pixels, I evaluate four metrics: the overall accuracy (OA) for all the classes and precision (P), recall (R), and F1-score (F1) for the forest class (FOR). In the latter case, I refer to a binary problem by considering as reference the NDVI mask and the classes *forest* (FOR) and *others* (OTH). On the one hand, the overall accuracy of eq.(3.16) measures the performance of the classification model. On the other hand, the remaining three metrics refer to the model's effectiveness in recognizing a specific class, in this case, the FOR class. Precision (P) and recall (R) are respectively defined as:

$$P = \frac{TP}{TP + FP}, \tag{3.19}$$

and

$$R = \frac{TP}{TP + FN}. \tag{3.20}$$

The precision and recall determine the cost of a false alarm and the classifier's capability to detect a forest pixel correctly, respectively. The F1-Score, eventually, aggregates the latter two measures to give a summary score and is defined as follows:

$$F1 = \frac{2 \cdot P \cdot R}{P + R}. \tag{3.21}$$

The F1-Score reaches its maximum at 1 when precision and recall are 1. It can be interpreted as a weighted average of precision and recall and considers both false positives and false negatives.

Sentinel-2 for monthly validation

Sentinel-2 images are used as an external reference for validating the monthly forest/non-forest classification over specific regions of interest. In particular, I consider two aspects of the vegetation, which can be translated into vegetation indexes derived from multispectral data: plant health and water stress. Indeed, vegetation absorbs solar radiation in different bands and scatters backward a different percentage of it. The percentage of reflected radiation in specific bands, such as near-infrared (NIR), red (RED), and short-wave infrared (SWIR), concurs to the definition of the following two different vegetation indices: (1) the NDVI, i.e., the Normalized Difference Vegetation Index, and (2) the NDMI, which stands for Normalized Difference Moisture Index.

The former describes the vigor level of a vegetated area, and it is calculated as the ratio between the difference and the sum of the reflected radiations in the near-infrared and the red channels:

$$\mathrm{NDVI} = \frac{\mathrm{NIR} - \mathrm{RED}}{\mathrm{NIR} + \mathrm{RED}} = \frac{\mathrm{B08} - \mathrm{B04}}{\mathrm{B08} + \mathrm{B04}}. \tag{3.22}$$

NIR stands for the near-infrared band and falls roughly between 760 and 900 nanometers, and RED is the visible red channel from 650 to 680 nanometers, corresponding using Sentinel-2 to band 8 (B08) and band 4 (B04), respectively. The NDVI varies between -1 and 1. Considering that the rainforest may be explained as an area with high canopy cover and high vigor, I created a forest/non-forest map by setting all those pixels with NDVI higher than 0.7 as forest. Differently, the NDMI is an informative index used to determine vegetation water content. It is calculated as the ratio between the difference and the sum of the reflected radiations in the near-infrared and short-wave infrared bands:

$$\mathrm{NDMI} = \frac{\mathrm{NIR} - \mathrm{SWIR}}{\mathrm{NIR} + \mathrm{SWIR}} = \frac{\mathrm{B08} - \mathrm{B11}}{\mathrm{B08} - \mathrm{B11}}. \tag{3.23}$$

SWIR is the Short-Wave Infrared band, which typically ranges from 1550 to 1750 nanometers. Although the NDMI was initially developed for use with Landsat Thematic Mapper (TM) bands 4 (NIR) and 5 (SWIR), I replicate it using Sentinel-2 bands 8 (B08) and 11 (B11) [66]. In this work, the NDMI is used together with the RGB image to evaluate the results visually. Furthermore, because of the strong dependency of Sentinel-2 data on clouds and cloud shadows, I generate a different mask, that I call *Unclassified mask*, valid for the measure of the cloud cover percentage of each acquisition. In particular, this mask is obtained by merging the cloud, and the cloud shadow layers inside the Scene Classification (SCL) map, a thematic map freely available in the Sentinel-2 Level-2A products [67]. In particular, I define for this mask three different classes: the missing data pixels (MDA), the valid pixels (VAL) and the unclassified data (UNC), i.e. clouds (dense and medium cirrus) and cloud shadows. Given a set of *Unclassified masks*, I select the mostly cloudless Sentinel-2 acquisition, i.e., the optical image whose cloud cover percentage is the minimum one within the Sentinel-1 stack observation time. The presented methodology can be schematized as in Figure 10.

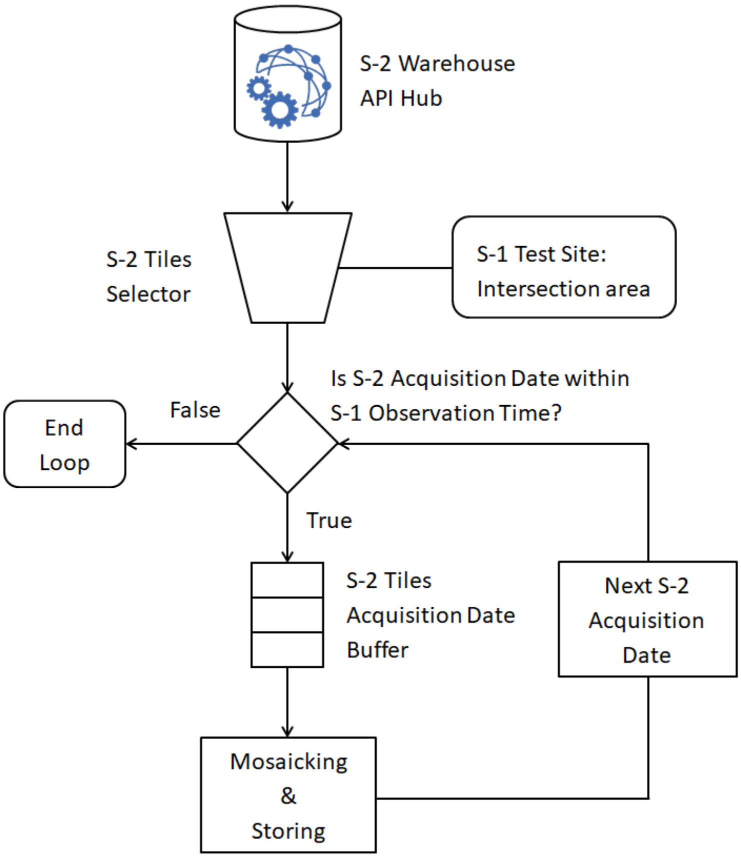

Figure 10: Block processing scheme for the automatic generation of Sentinel-2 mosaicked images over the region of interest.

During the downloading of the Sentinel-2 tiles, a first selection is applied to consider only those Sentinel-2 acquisitions whose footprint falls within the test site region, previously fixed in the Sentinel-1 processing chain of Figure 6. Then a for loop loads in a buffer all the available tiles and merges them using a mosaicking algorithm. Finally, it stores the result, i.e., the strip associated with the acquisition date. The loop continues until the complete span of all Sentinel-2 acquisition dates within the Sentinel-1 observation time. The result is a stack of Sentinel-2 mosaicked images covering the Sentinel-1 test site. The main benefit of this approach is the possibility to automatically select the most cloudless Sentinel-2 acquisition, i.e., the one with the lowest cloud cover percentage, given the coordinates of a smaller region of interest in the test site. Figure 11 shows an example of the results generated by the above-mentioned automatic system over a dedicated patch. In this specific case, the algorithm estimates a cloud cover percentage of 22.40% over the patch.

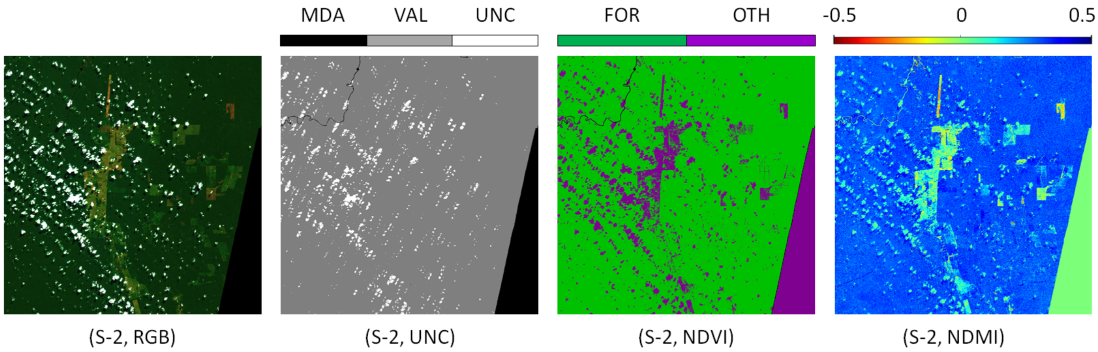

Figure 11: Examplary results for the pre-processing of Sentinel-2 data. From left to right: (S-2, RGB) is the True Color map; (S-2, UNC) is the *Unclassified mask*; (S-2, NDVI) is the NDVI mask; (S-2, NDMI) is the NDMI index.

3.2.5 Deep Learning approaches

The above methodologies have concentrated on exploiting Sentinel-1 time series by focusing on processing aspects and modeling the temporal decorrelation for specific land cover classes. This project has further committed to improving the performance of previously presented methodologies. In particular, the one related to the spatial and temporal resolution of the end-product. To do so, I investigated DL methodologies to better process the data. On the one hand, I focused on improving the interferometric phase and coherence estimation. Deep residual models, as the Φ-Net [6], can generate accurate coherence maps without resolution degradation.

On the other hand, classification improvement has been targeted. A U-Net model has been used in place of the RF classifier. The same framework can be used for single coherence image classification. In this way it will be possible to generate one forest map from a single coherence image and shorten the mapping interval to 6 days. The coherence in place of the temporal decorrelation is less reliable, and one can recoup the performance by using DL-based semantic segmentation approaches.

Interferometric parameters estimation with the Φ-Net

The proposed Φ-Net is a DL residual model to estimate InSAR parameters. This approach allows obtaining a coherence map with almost no degradation of the input data resolution. The Φ-Net is trained using synthetic data obtained by an innovative strategy based on the theoretical modeling of the physics behind the SAR acquisition principle. The peculiarity of the employed strategy is that it allows the network to generalize the estimation problem with respect to different noise levels, the nature of the imaged target on the ground, and the acquisition geometry. Figure 12 shows the network architecture. For a detailed description of the Φ-Net I refer to [6].

As an example, in the following, I show the comparison between the data filtered with the proposed initially moving average for a 50×50 meters posting and the new result obtained with the Φ-Net.

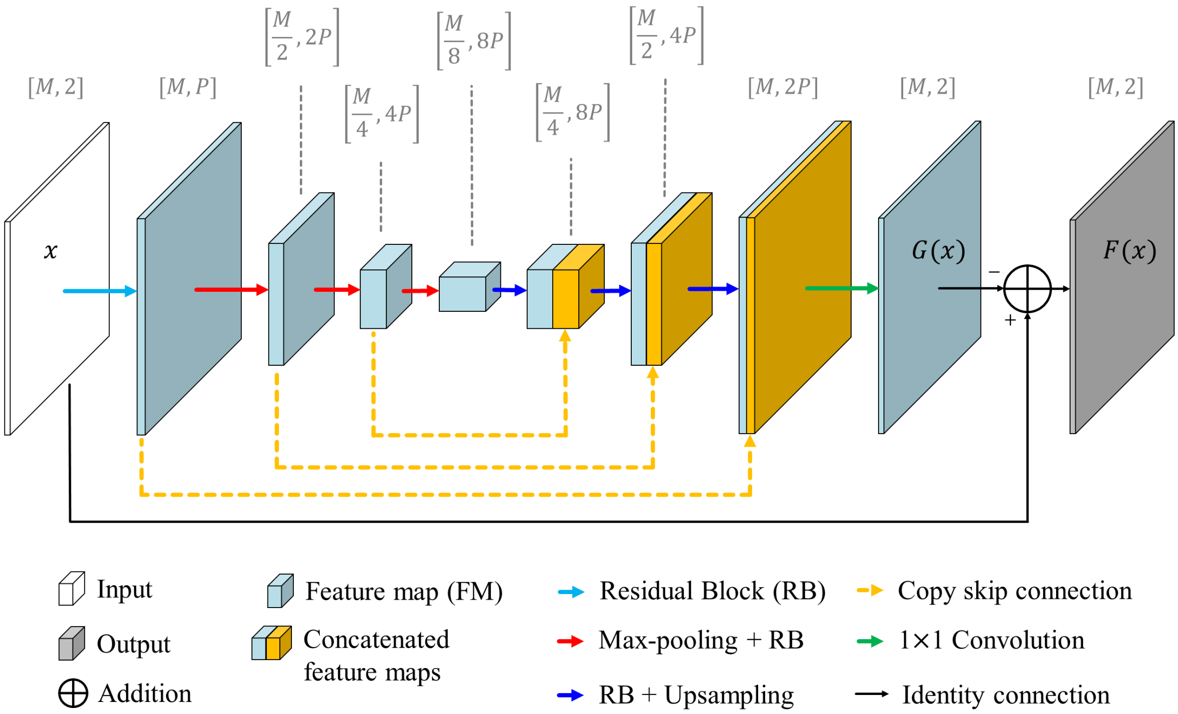

Figure 12: Φ-Net network architecture. The structure of the residual blocks is depicted in Figure 13.

The coherence estimated with this method can allow the production of forest maps at 10×10 meters posting grid. Further evaluations and comparisons are left for future research investigations.

Forest mapping with DL-based semantic segmentation

As seen so far, the retrieval of the temporal decorrelation can primarily improve the classification performance since it is less subject to noise and temporal non-stationarity in the scene. As a drawback, such an approach is computationally demanding since it requires the computation of the full coherence map for each pixel on the ground. Furthermore, it also implies that the acquisition with the largest temporal baseline is acquired, which for the proposed methodology is one month.

In this project, I further investigated using a DL model for semantic segmentation to improve classification performance. The used model is the one already proposed in [68] and depicted in Figure 15. For this analysis, I used as input features the multi-temporal backscatter γ^0, the incidence angle θ_{inc}, the decorrelation constant τ, and the long-term coherence ρ_{LT}. The training and test dataset are the same used for the forest mapping presented in Section 3.2.3.

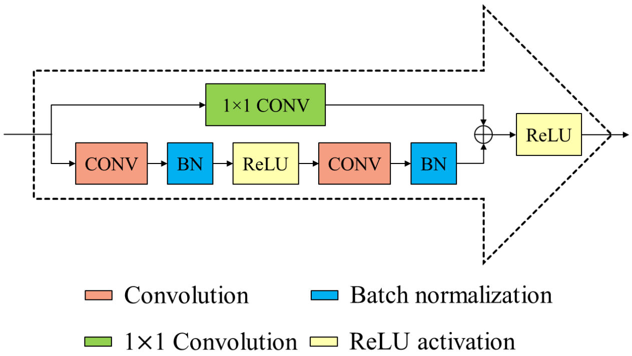

Figure 13: Φ-Net residual block operations.

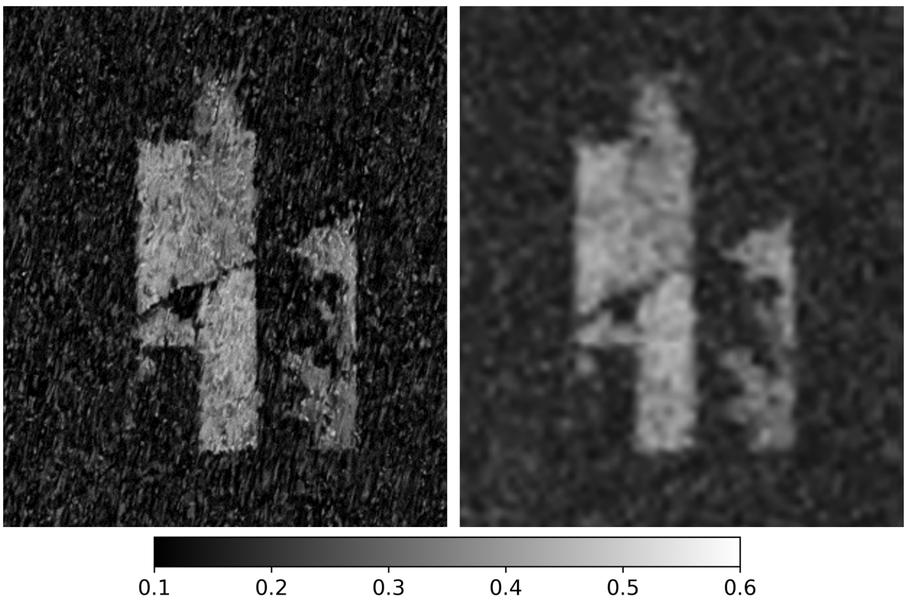

Figure 14: Comparison between coherence maps at 10×10 meters posting resulting from the Φ-Net (left) and the classical moving average (right).

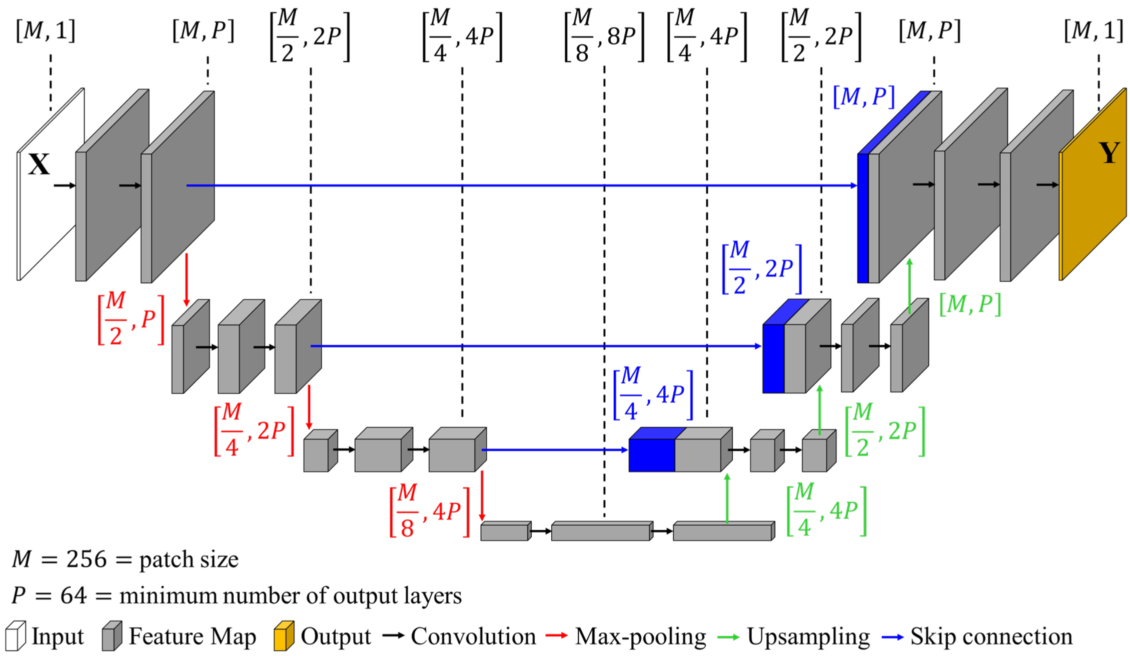

Figure 15: U-Net semantic segmentation model for forest mapping.

3.3 Data

In the following, I describe all the used Sentinel-1 datasets for the performed analysis. In addition, I also indicate the reference data sets and third-party data.

3.3.1 Europe dataset

The first data set that I considered for the analysis and test of the land cover classification methodology proposed in [46] has been over Europe, where both Sentinel-1a and -1b acquisitions are present. Indeed, for a more precise estimation of the temporal decorrelation, a revisit time of 6 days is favorable. The selected area covers about 700×500 km and is depicted in Figure 16.

Specifically, the data set is composed of seven stacks of Sentinel-1 IW scenes (VV polarization channel), each of those comprising 6 acquisitions characterized by a revisit time of 6 days and covering an overall period of one month (August 2018). The acquisition orbits, dates, and geographical coordinates of the utilized stacks are summarized in Table 2. Each input IW image, composed of three sub-swaths, covers a swath of 250 km length at a resolution of 14×3.7 meters in the azimuth and ground range dimensions.

Table 2: Sentinel-1 data set over central Europe (Germany). Data download has been performed through `https://scihub.copernicus.eu/`. For each stack, the symbol * indicates the primary image.

	Stack 1	**Stack 2**	**Stack 3**	**Stack 4**	**Stack 5**	**Stack 6**	**Stack 7**
orbit	139	139	139	168	168	168	168
region	Baden-Württemberg	Rheinland-Palatinate	Nord Rhein-Westphalen	Bayern	Thüringen	Sachsen	Mecklenburg-Vorp.
Abbrev.	BW	RP	NW	BY	TH	SN	MV
Image	**Acquisition dates**						
1	2018.08.01	2018.08.01	2018.08.01	2018.07.28	2018.07.28	2018.07.28	2018.07.28
2	2018.08.07	2018.08.07	2018.08.07	2018.08.03	2018.08.03	2018.08.03	2018.08.03
3	2018.08.13*	2018.08.13*	2018.08.13*	2018.08.09	2018.08.09	2018.08.09	2018.08.09
4	2018.08.19	2018.08.19	2018.08.19	2018.08.15*	2018.08.15*	2018.08.15*	2018.08.15*
5	2018.08.25	2018.08.25	2018.08.25	2018.08.21	2018.08.21	2018.08.21	2018.08.21
6	2018.08.31	2018.08.31	2018.08.31	2018.08.27	2018.08.27	2018.08.27	2018.08.27
	Corner Coordinates [deg]						
lat min	47.9676283	49.4508966	50.9358976	47.9499978	49.4358306	50.9199976	52.4016654
lat max	49.4748923	50.9608575	52.4458574	49.9545851	51.4413178	52.9263836	54.4098489
lon min	5.238333	5.5870266	5.9489214	9.3441662	9.6941661	10.0491661	10.4188564
lon max	8.9128063	9.3759577	9.8550366	13.1737098	13.6414315	14.1314738	14.6397917

External reference: the CORINE land cover map

As a ground truth reference for land cover, I exploited the CORINE Land Cover (CLC) map, updated to the year 2012 [69]. It consists of 44 land cover classes generated by visual inspection from IRS P6 LISS III and RapidEye satellite data. The product has a pixel spacing of 100×100 meters and an accuracy higher than 85%. For the purposes of the present investigation, I grouped such classes into four higher-level classes, as shown in the last column of Table 3: *artificial surfaces* (ART), *forests* (FOR), *non-forested areas* (NFR), and *water bodies and invalid or no data* (INV). I used the first three higher-level classes to perform the classification, while the last one, which includes water and invalid pixels, has been masked out.

Table 3: Class grouping from CLC (ART: *artificial surfaces*, FOR: *forests*, NFR: *non-forested areas*, INV: water bodies and invalid or no data).

CLC Labels			
Label 1	**Label 2**	**Label 3**	**Higher-level class**
Artificial surfaces	Urban fabric	Continuous urban fabric	
Artificial surfaces	Urban fabric	Discontinuous urban fabric	
Artificial surfaces	Industrial, commercial and transport units	Industrial or commercial units	
Artificial surfaces	Industrial, commercial and transport units	Road and rail networks and associated land	
Artificial surfaces	Industrial, commercial and transport units	Port areas	
Artificial surfaces	Industrial, commercial and transport units	Airports	**ART**
Artificial surfaces	Mine, dump and construction sites	Mineral extraction sites	
Artificial surfaces	Mine, dump and construction sites	Dump sites	
Artificial surfaces	Mine, dump and construction sites	Construction sites	
Artificial surfaces	Artificial, non-agricultural vegetated areas	Green urban areas	
Artificial surfaces	Artificial, non-agricultural vegetated areas	Sport and leisure facilities	
Forest and semi natural areas	Forests	Agro-forestry areas	
Forest and semi natural areas	Forests	Agro-forestry areas	**FOR**
Forest and semi natural areas	Forests	Coniferous forest	
Agricultural areas	Arable land	Non-irrigated arable land	
Agricultural areas	Arable land	Permanently irrigated land	
Agricultural areas	Arable land	Rice fields	
Agricultural areas	Permanent crops	Vineyards	
Agricultural areas	Permanent crops	Fruit trees and berry plantations	
Agricultural areas	Permanent crops	Olive groves	
Agricultural areas	Pastures	Pastures	
Agricultural areas	Heterogeneous agricultural areas	Annual crops associated with permanent crops	
Agricultural areas	Heterogeneous agricultural areas	Complex cultivation patterns	
Agricultural areas	Heterogeneous agricultural areas	Land principally occupied by agriculture...	
Agricultural areas	Heterogeneous agricultural areas	Agro-forestry areas	
Forest and semi natural areas	Scrub and/or herbaceous veg. associations	Natural grassland	
Forest and semi natural areas	Scrub and/or herbaceous veg. associations	Moors and heathland	**NFR**
Forest and semi natural areas	Scrub and/or herbaceous veg. associations	Sclerophyllous vegetation	
Forest and semi natural areas	Scrub and/or herbaceous veg. associations	Transitional woodland-shrub	
Forest and semi natural areas	Open spaces with little or no vegetation	Beaches, dunes, sands	
Forest and semi natural areas	Open spaces with little or no vegetation	Bare rocks	
Forest and semi natural areas	Open spaces with little or no vegetation	Sparsely vegetated areas	
Forest and semi natural areas	Open spaces with little or no vegetation	Burnt areas	
Forest and semi natural areas	Open spaces with little or no vegetation	Glaciers and perpetual snow	
Wetlands	Inland wetlands	Inland marshes	
Wetlands	Inland wetlands	Inland marshes	
Wetlands	Inland wetlands	Peat bogs	
Wetlands	Maritime wetlands	Salt marshes	
Wetlands	Maritime wetlands	Salines	
Wetlands	Maritime wetlands	Intertidal flats	
Water bodies	Inland waters	Water courses	
Water bodies	Inland waters	Water bodies	
Water bodies	Marine waters	Coastal lagoons	
Water bodies	Marine waters	Estuaries	
Water bodies	Marine waters	Sea and ocean	**INV**
NODATA	NODATA	NODATA	
UNCLASSIFIED	UNCLASSIFIED LAND SURFACE	UNCLASSIFIED LAND SURFACE	
UNCLASSIFIED	UNCLASSIFIED WATER BODIES	UNCLASSIFIED WATER BODIES	
UNCLASSIFIED	UNCLASSIFIED	UNCLASSIFIED	

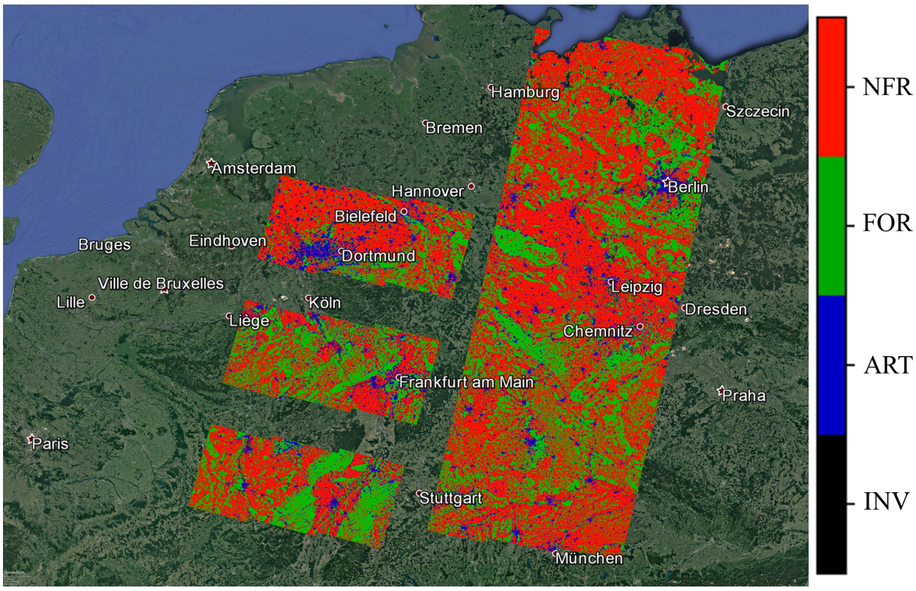

Figure 16: Reference CLC land cover map for the considered European sites, with classes grouped according to Table 2.

3.3.2 Amazon rainforest dataset

For the forest mapping application, I selected a study area over the Rondonia state, Brazil, approximately 238 thousand km^2 large. The area is positioned between 7°50′ and 13°50′ latitude South and 59°50′ and 67°10′ longitude West. This area, situated along the Amazon's deforestation arch, has become of primary interest during recent years since most deforested events occurred. For this reason, since April 2019, the European Space Agency (ESA) has planned an experimental 6-days repeat-pass coverage obtained with the combined operation of Sentinel-1a and Sentinel-1b satellites. The employed data set comprises 12 Sentinel-1 time series. The corresponding FROM-GLC reference map is shown superimposed to Google Earth in Figure 18.

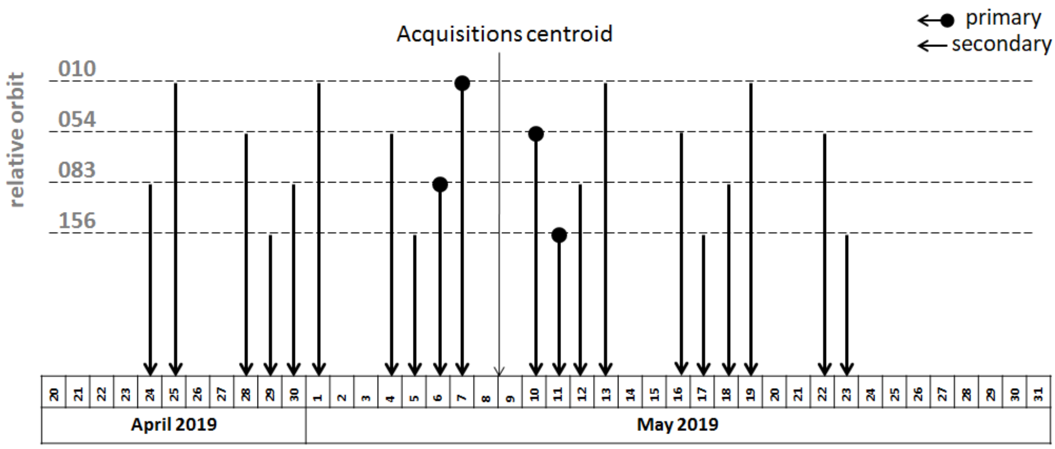

Figure 17: Sentinel-1 time series description: acquisition dates. A dot represents the primary image, while the arrows indicates the secondary images.

Table 4: Sentinel-1 time series description: locations. From left to right: stack number, relative orbit number, name of the time series associated with the orbit number, corner coordinates in latitude and longitude. The asterisks mark the test dataset.

			Corner Coordinates [deg]			
Stack	**Orbit**	**Name**	**Lat. min**	**Lat. max**	**Lon. min**	**Lon. max**
1	010	TS_0	$9^{\circ}40'58.34"S$	$7^{\circ}42'53.99"S$	$59^{\circ}52'18.71"W$	$61^{\circ}44'43.20"W$
2	010	TS_1	$11^{\circ}16'36.74"S$	$9^{\circ}15'31.41"S$	$60^{\circ}12'59.94"W$	$62^{\circ}5'1.52"W$
3	010	TS_2	$12^{\circ}45'21.09"S$	$10^{\circ}43'21.81"S$	$60^{\circ}33'23.20"W$	$62^{\circ}26'23.22"W$
4	010	TS_3	$14^{\circ}10'32.67"S$	$12^{\circ}12'43.74"S$	$60^{\circ}53'48.14"W$	$62^{\circ}46'54.92"W$
5	054	TS_0	$10^{\circ}12'15.96"S$	$8^{\circ}4'40.60"S$	$66^{\circ}8'34.73"W$	$67^{\circ}59'40.25"W$
6*	083	TS_0	$8^{\circ}51'9.51"S$	$6^{\circ}50'56.20"S$	$61^{\circ}42'32.10"W$	$63^{\circ}36'0.35"W$
7*	083	TS_1	$10^{\circ}22'8.36"S$	$8^{\circ}32'54.94"S$	$62^{\circ}4'44.36"W$	$63^{\circ}37'30.02"W$
8*	083	TS_2	$11^{\circ}51'16.77"S$	$10^{\circ}2'26.15"S$	$62^{\circ}25'15.09"W$	$64^{\circ}19'5.05"W$
9*	083	TS_3	$13^{\circ}24'3.87"S$	$11^{\circ}32'42.18"S$	$62^{\circ}44'38.52"W$	$64^{\circ}40'34.71"W$
10	156	TS_0	$9^{\circ}24'34.67"S$	$8^{\circ}4'15.76"S$	$63^{\circ}53'30.37"W$	$65^{\circ}56'1.88"W$
11	156	TS_1	$10^{\circ}15'7.76"S$	$8^{\circ}48'35.78"S$	$64^{\circ}5'7.05"W$	$66^{\circ}8'22.17"W$
12	156	TS_2	$10^{\circ}36'21.14"S$	$9^{\circ}46'22.31"S$	$64^{\circ}9'39.68"W$	$66^{\circ}19'6.56"W$

Test area for deforestation monitoring: southern Brazilian Amazon

For change detection purposes, a large region of about 44 million hectares highlighted in red in Figure 19 and located in the southern Brazilian Amazon has been considered. The test area comprises the state of Rondonia, the eastern side of Acre, and a small area close to Boca do Acre, a municipality in the state of Amazonas, where recurrent deforestation activity is present. Indeed, this region is of general interest since it is part of the Amazonian *arc of deforestation*, a belt of rapidly disappearing tropical forest that follows the southern margin of the Amazon and bends northeastward toward the bank of the Amazon River mouth.

Figure 19: Google Earth image over the Amazon basin with in red the test site location.

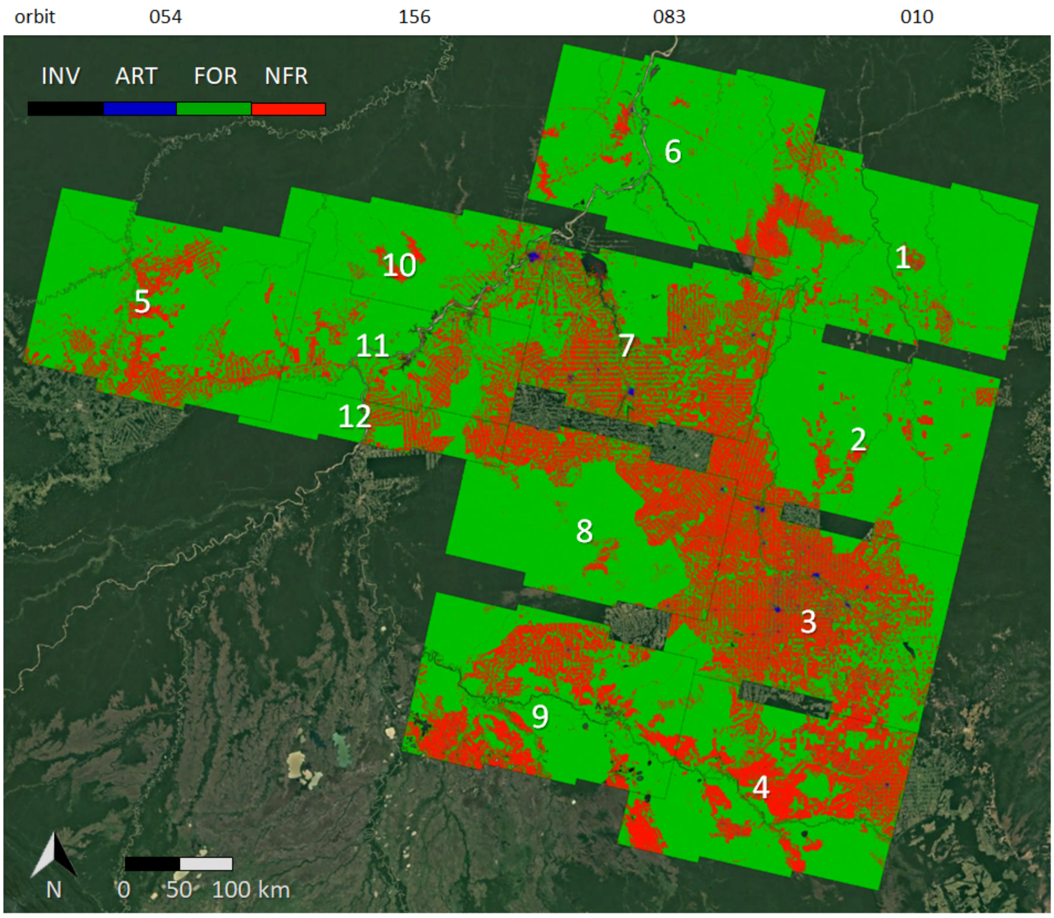

Figure 18: Finer Resolution Observation and Monitoring of Global Land Cover (FROM-GLC, 2017) map chosen as ground truth.

To monitor the state of the rainforest in the southern Amazon, the European Space Agency (ESA) planned, between the end of April 2019 and the end of December 2019, a denser SAR coverage using Sentinel-1A and Sentinel-1B satellites over such an area, reaching a constant repeat cycle of 6 days. Accordingly, for testing the change detection algorithm, I use 3 Sentinel-1 time series over footprint number 5, acquired in three consecutive months: May, June, and July 2019, respectively. Figure 20 shows the acquisitions dates of the complete dataset of Sentinel-1 data considered.

The square and circular markers identify which sensor, between S-1A and S-1B, acquires on a specific date. Each relative orbit number within a given month is highlighted with a different color and contains a different number of footprints. Furthermore, the footprints associated with a relative orbit number and analyzed on a precise observation time have the same reference acquisition (primary image) for performing the multi-temporal coregistration.

FROM-GLC and PRODES reference maps

As done for the Europe data set, the FROM-GLC map, which comprises an inventory of 10 land cover classes, has been grouped into four macro-classes with higher semantic: artificial

Table 5: FROM-GLC classes aggregation. (ART) artificial surfaces. (FOR) forests. (NFR) non-forested areas. (INV) invalids.

FROM-GLC	**Higher-level class**
Unclassified Water Snow/Ice	**INV**
Impervious surface	**ART**
Forest	**FOR**
Cropland Grassland Shrubland Wetland Tundra Bareland	**NFR**

surfaces (ART), forests (FOR), non-forested areas (NFR), and water bodies and unclassified or no data as invalids (INV), as shown in Table 5. Furthermore, all the possible temporal inconsistencies in the FROM-GLC reference map due to temporal changes have been discarded by relying on the PRODES (Programa de Cálculo do Desflorestamento da Amazônia) digital map [70]. PRODES consists of a ground polygon inventory over the Amazon rainforest, updated yearly with the latest detected deforestation areas. It is a medium-resolution ($30\,m$) product derived from visual inspection of optical data and does not identify changes within areas that are smaller than $6.25\,ha$ [71].

I extract the polygons corresponding to new clear-cuts between 2017 and 2019 by using different updates of the PRODES map. These sets are used in [59] and [63] to evaluate the classification performance of the forest maps and to extract the yearly clear-cuts as the difference between clearing areas detected by PRODES in 2018 and 2019 separately.

3.3.3 Third-part data: TanDEM-X/PAZ acquisitions

For the analysis of volume and temporal decorrelation at X band, I considered five test sites, each one characterized by the presence of different land cover classes and located over:

- Demmin (Germany)
- Salar de Uyuni (Bolivia)
- Amazonas (Brazil)
- Skövde (Sweden)
- Greenland

For each test site, I utilized TDM-PAZ interferometric time series in horizontal (HH) polarization, acquired in an overall period that goes from May 2019 up to December 2020. A

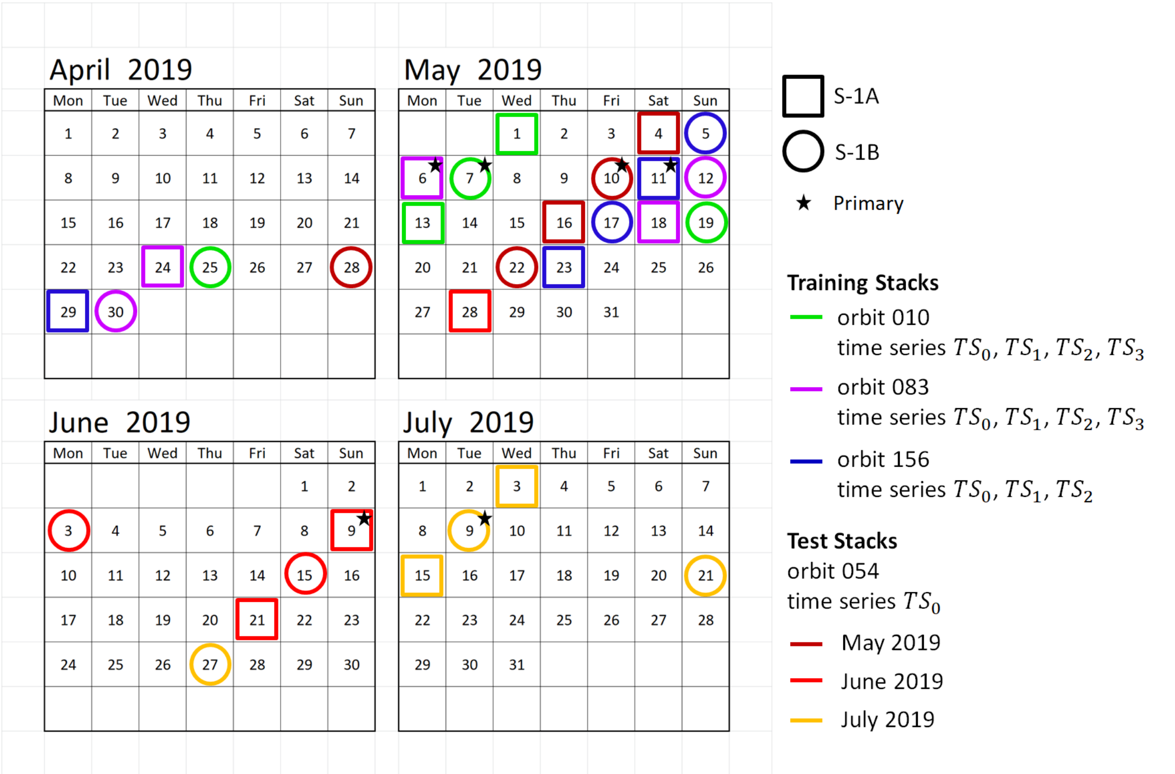

Figure 20: Sentinel-1 acquisition description. A star represents the primary image, while squares and circles indicate Sentinel-1A and -1B secondary images. The colors identify different months.

summary of the used time series, together with their main acquisition parameters and land cover classes per test site, is presented in Table 6.

Moreover, to retrieve the long-term coherence, I use additional TDM acquisitions with a very long temporal baseline, which are marked with an asterisk in Table 6.

Table 6: TDM-PAZ time series description. LC - land cover. θ_{inc} - mean incidence angle. Platform - TDM or PAZ. AIID - Acquisition Item ID. Date - acquisition date. * - TDM acquisitions with long temporal baselines.

Demmin			**Salar de Uyuni**			**Amazonas**			**Skövde**			**Greenland**		
LC: *Crops* (CRP), *Grasses* (GRS), *Urban* (URB)			LC: *Soil and rocks* (SOL)			LC: *Rainforest* (RFR)			LC: *Boreal forest* (BRF)			LC: *Ice and snow* (ICE)		
$\theta_{\text{inc}} = 38°$			$\theta_{\text{inc}} = 48°$			$\theta_{\text{inc}} = 41°$			$\theta_{\text{inc}} = 34°$			$\theta_{\text{inc}} = 42°$		
Platform	AIID	Date	Platform	AIID	Date	Platform	AIID	Date	Platform	AIID	Date	Platform	AIID	Date
PAZ	15481	2019.09.10	PAZ	18316	2019.11.23	TDM	1600801	2019.05.17	PAZ	12123	2019.05.17	PAZ	14368	2019.08.10
TDM*	1641717	2019.09.17	TDM	1654786	2019.11.30	PAZ	12185	2019.05.21	TDM*	1600791	2019.05.24	TDM	1634742	2019.08.17
PAZ	15895	2019.09.21	PAZ	18754	2019.12.04	TDM	1600800	2019.05.28	PAZ	12394	2019.05.28	PAZ	14749	2019.08.21
TDM	1641657	2019.09.28	TDM	1654718	2019.12.11	PAZ	12444	2019.06.01	PAZ	15861	2019.09.15	TDM	1634656	2019.08.28
TDM*	1600895	2019.05.19	PAZ	19243	2019.12.15	TDM*	1600799	2019.06.08	TDM*	1641694	2019.09.22	PAZ	15129	2019.09.01
			TDM*	1416699	2017.03.26	PAZ	12776	2019.06.12	PAZ	16297	2019.09.26	TDM*	1638751	2019.09.08
			PAZ*	12186	2019.05.20	TDM	1600798	2019.06.19				PAZ	15490	2019.09.12
						PAZ	13054	2019.06.23				TDM	1640676	2019.09.19
						PAZ	15524	2019.09.08				PAZ	15906	2019.09.23
						TDM*	1641721	2019.09.15				TDM	1640756	2019.09.30
						PAZ	15921	2019.09.19				TDM*	1599773	2019.05.10

3.4 Results

This section summarizes the results obtained from all the proposed methodologies. The results are presented in the same order used in the methodological part. While I provide some sample results in the following, I refer to the published articles and provide the corresponding references.

3.4.1 Land cover classification in Europe

This section shows the results obtained by applying the framework for Sentinel-1 time series explained in Section 3.2.2 over the Europe dataset described in Section 3.3.1. I will first exhibit preliminary analysis results on the estimated multi-temporal interferometric parameters. Consequently, I show the results obtained from the classification and assess the performance with respect to the modified CLC external reference shown in Section 3.3.1.

I present the analysis and the classification results obtained by applying the algorithm to the Sentinel-1 stacks 1-6 in Table 2. While here I summarize the performed experiments, a complete description of the performed work is to be found in [46].

Analysis on the estimated parameters

The normalized histograms of the estimated quantities $\hat{\gamma}^0$, $\hat{\rho}_{\text{LT}}$, and $\hat{\tau}$ are depicted in Figure 21 (a) to (c) for each land cover class, separately. One can observe from these histograms that the distributions of $\hat{\gamma}^0$ and $\hat{\tau}$ can be approximated by mono-modal Gaussian-like distributions with well separable mean values but with a significant overlapping. Differently, the distributions of $\hat{\rho}_{\text{LT}}$ for the classes *forests* (FOR) and *non-forested areas* (NFR) are largely superimposed, while a high degree of separation is visible between *artificial surfaces* (ART) and all other classes.

Figure 21 (d) shows the derived models of the temporal decorrelation factor $\hat{\rho}_{\text{temp}}$ in eq.(3.8), obtained by applying the mean values of the distributions of $\hat{\rho}_{\text{LT}}$ and $\hat{\tau}$. As expected, the *artificial surfaces* (ART) class decorrelates much less than the other two classes. It is due to the intrinsic nature of artificial scatterers, whose radar cross-section and phase are more stable in time with respect to distributed ones.

It has to be noted that meaningful use of multiple features as input to a generic classifier requires a low degree of correlation. I compute the bi-dimensional histograms of all possible

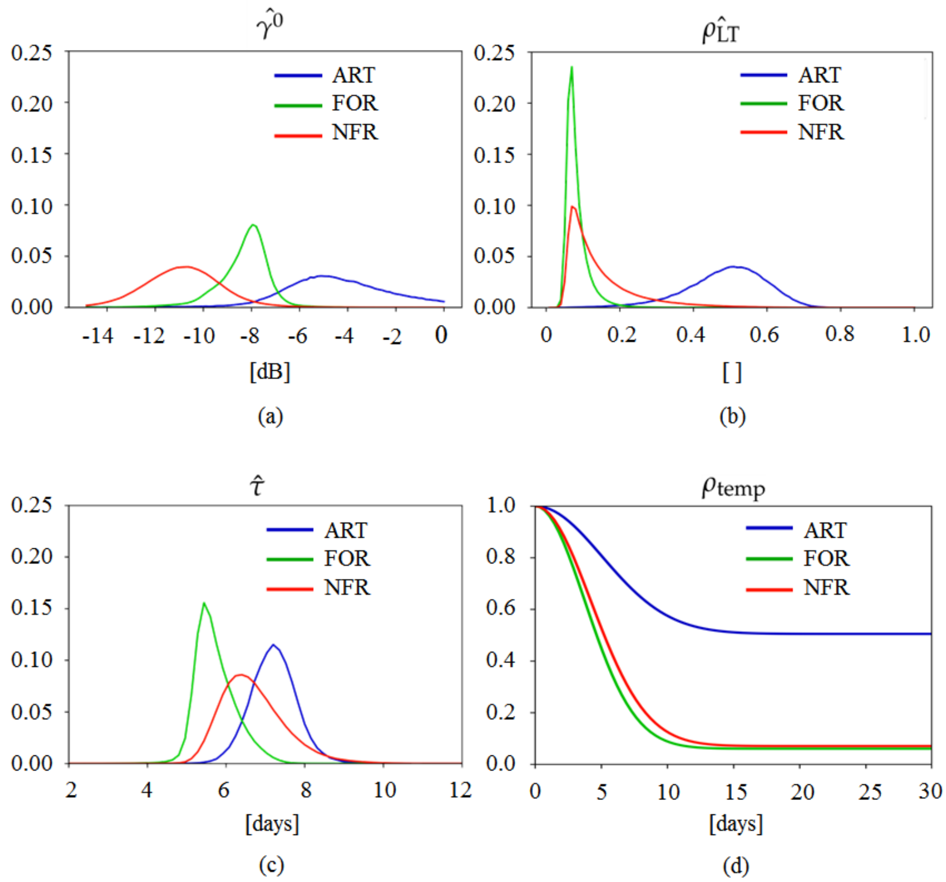

Figure 21: Normalized histograms for the different estimated quantities and classes. (a) temporal multi-looked backscatter $\hat{\gamma}^0$. (b) long-term coherence $\hat{\rho}_{\mathrm{LT}}$ (c) decorrelation constant $\hat{\tau}$ (d) Exponential model of the volume decorrelation factor, derived using the mean values of $\hat{\rho}_{\mathrm{LT}}$ and $\hat{\tau}$ distributions.

parameter combinations for each land cover class to verify this aspect. The results are depicted in Figure 22, and from the histogram's orientation, no relevant correlation between features is observed.

Classification results and performance analysis

In the following, I show the results obtained by applying the algorithm described in Section 3.2.2 and analyze its performance in the proposed three different cases, characterized by different features as input to the RF classifier:

- *case 1*: $\hat{\gamma}^0$ and θ_{inc},
- *case 2*: $\hat{\tau}$, $\hat{\rho}_{\mathrm{LT}}$, and θ_{inc},
- *case 3*: $\hat{\gamma}^0$, $\hat{\tau}$, $\hat{\rho}_{\mathrm{LT}}$, and θ_{inc}.

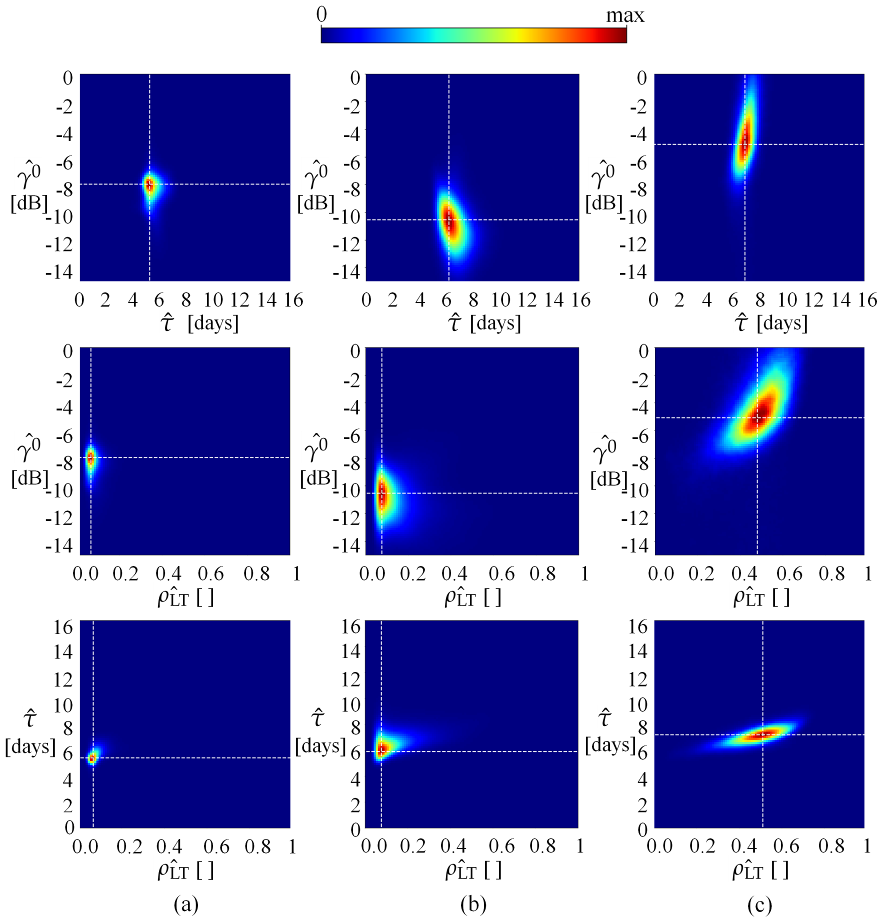

Figure 22: Normalized two-dimensional histograms of $\hat{\gamma}^0$, $\hat{\tau}$, and $\hat{\rho}_{\text{LT}}$, for the three considered land cover classes.

Figure 23 shows the derived classification map from stack 1 for *case 3*, where both backscatter and interferometric parameters are used as input features.

It is worth mentioning that a significant improvement in terms of classification accuracy has been observed by increasing the n_{est} and $leaf_{size}$ in the RF algorithm, up to a saturation level after which its performance stabilizes. The chosen values of n_{est} and $leaf_{size}$ equal to 50 are, on the one hand, close to such a saturation level, and on the other hand, a good compromise in terms of computational costs.

In the following, I show the results for three different patches highlighted in Figure 23 (yellow), which are depicted in details in Figure 24. The corresponding Google Earth optical images and the CLC reference are depicted in rows (i) and (ii), respectively. The crops in rows (iii) to (v) correspond to the three different cases introduced in Section 3.2.2, which differ from each other on the input features to the RF classifier (*case 1*, *case 2*, and *case 3*).

By using only the backscatter *case 1* (iii) the classifier tends to underestimate the *artificial surfaces* (ART) and the *forests* (FOR) classes in favor of the *non-forested areas* (NFR). This effect is prevalent in crop (a), but it can be observed in all the selected crops. Differently,

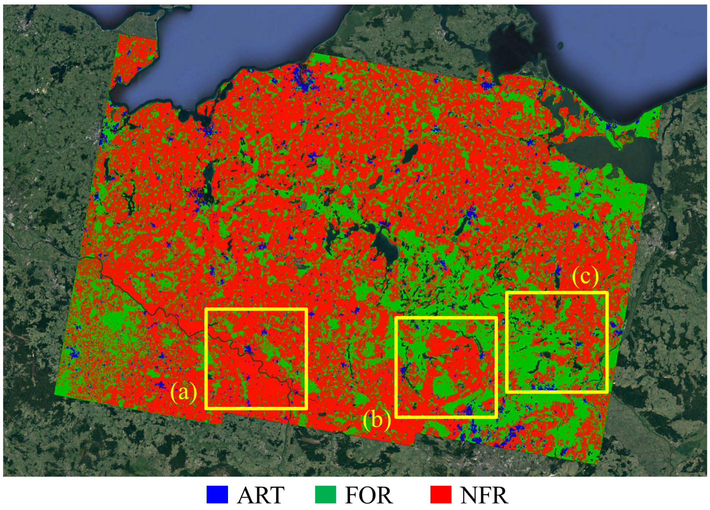

Figure 23: Derived classification map for the test set superimposed to Google Earth. Yellow polygons identify three selected patches displayed in detail in Figure 24.

Table 7: Classification overall accuracy OA for the three selected test patches and for 2 mln pixels randomly selected within the image (overall). Performance comparison between the three considered test cases.

input case	**patch (a)**	**patch (b)**	**patch (c)**	**overall**
case 1	76.02%	79.93%	76.86%	88.73%
case 2	79.30%	77.98%	71.43%	78.77%
case 3	83.28%	86.84%	82.9%	91.85%

by using the estimated interferometric parameters exclusively in *case 2* (iv), a more reliable behavior is observed for all the classes. It is observed for the crop (a) and (b), while the third crop shows some misclassification errors for the *non-forested areas* (NFR) class in favor of the *forests* (FOR) one. Finally, as expected, the combined use of backscatter and interferometric parameters (*case 3* (v)) performs better overall. Specifically, all classification errors are better solved in all crops.

Eventually, the performance is assessed as overall accuracy OA over the whole test dataset and selected patches in all considered cases. The results are summarized in Table 7 and confirm the considerations derived from the visual inspection of the classified patches. The results are presented in Table 7. As expected, the combined use of backscatter and interferometric parameters (*case 3*) shows the best performance by confirming the observations made with map visual inspection.

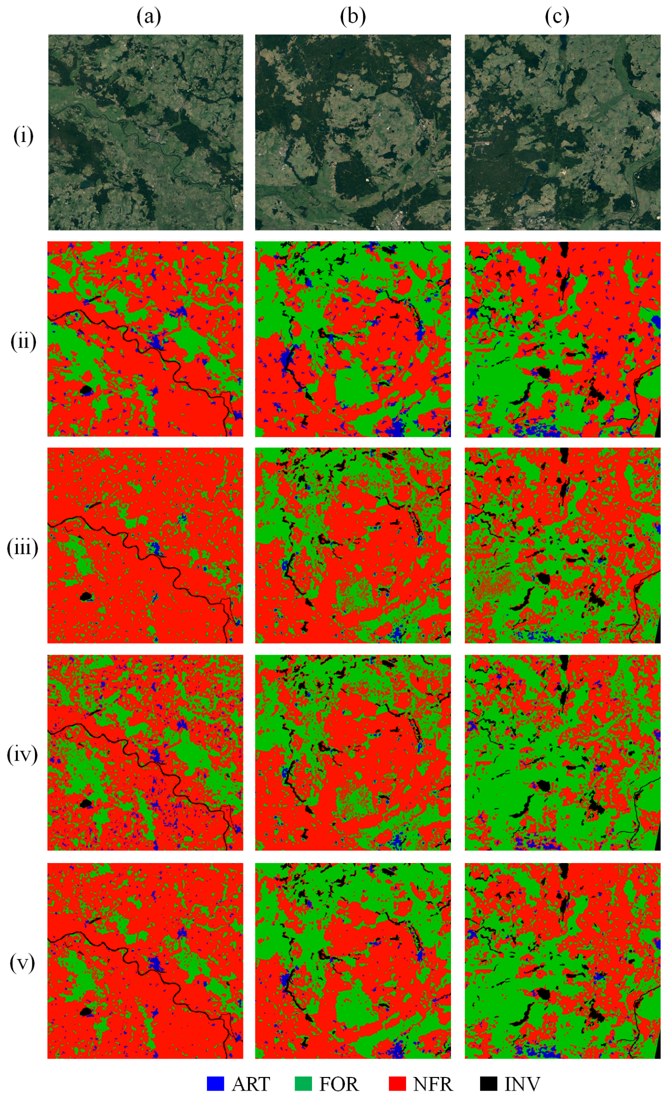

Figure 24: Sample patches (512×512 pixels) of three different locations from Figure 23. (row (i)) Google Earth optical image, (row (ii)) CLC reference Map, (rows (iii), (iv), and (v)) classification maps derived from Sentinel-1 stacks for *case 1* (iii), *case 2* (iv), and *case 3* (v).

3.4.2 Forest mapping

The experiments were conducted by splitting the twelve stacks of Table 4 into test and training swaths. The test set covers a strip of about 250 $km \times 1000$ km crossing the Rondonia state, as shown in Figure 25, and corresponds to the stacks of the relative orbit 83, marked with asterisks in Table 4. The remaining swaths were chosen for training the RF algorithm.

The first analysis is performed on a large-scale area, which is shown in Figure 25, where a comparison between the REF reference map and case *(SADH)* for the four swaths acquired with orbit number 83 is presented. The performance is evaluated in terms of overall accuracy (OA) and average accuracy (AA). Table 8 summarizes the two metrics for each of the four stacks, considering the set of inputs in case *(ORIG)* and in case *(SADH)*.

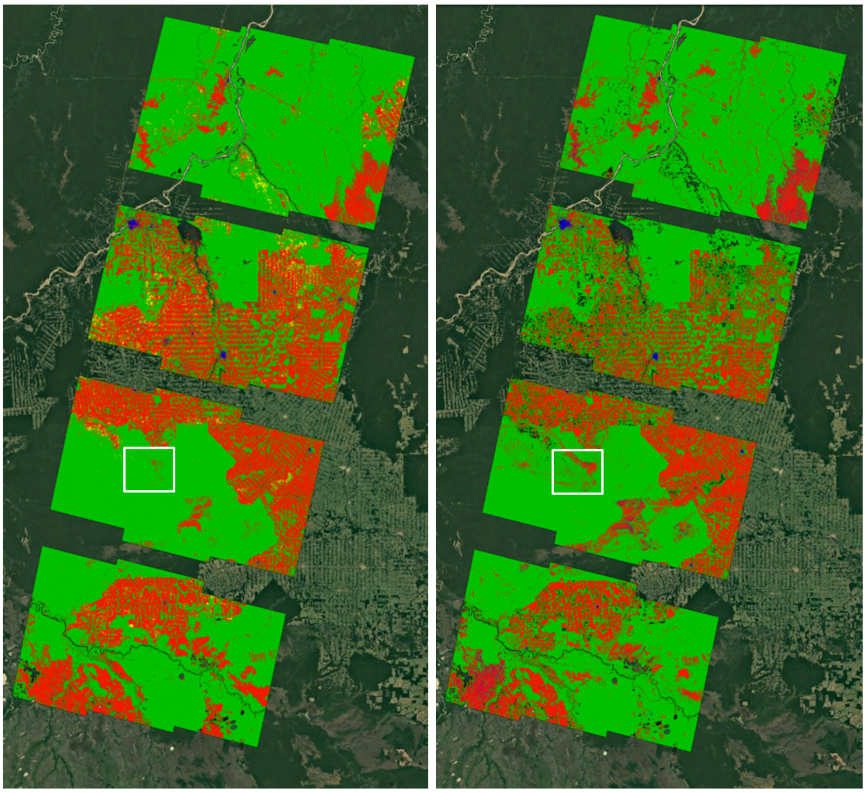

Figure 25: Comparison between the obtained classification result and the reference map.

All considered swaths are characterized by an overall accuracy above 82.50% and 84.26% for the *(ORIG)* and *(SADH)* cases, respectively, by considering all valid pixels within the images. Again, the additional information of the SADH textures increases both the OA and the AA by at least 1.5% in all four swaths. In particular, the RF improve its detection performance using the SADH textures. It is observed especially for the ART and NFR classes, depicted in blue and red, respectively, in Figure 25 and better visible with the analysis of the global confusion matrices in Figure 26.

Table 8: Overall accuracy (OA) and Average accuracy (AA) for the four swaths in Figure 25. Each swath is associated with a stack, according to the enumeration in Table 4.

	class	**stack 6**	**stack 7**	**stack 8**	**stack 9**
pixels	*ART*	10060	34890	6009	1054
	FOR	14626324	7846234	9822268	10087671
	NFR	1655335	6194973	4193972	4280135
case	**metric**	**stack 6**	**stack 7**	**stack 8**	**stack 9**
ORIG	*OA*	88.48%	82.50%	85.03%	84.84%
	AA	61.05%	81.64%	80.50%	71.95%
SADH	*OA*	91.90%	84.26%	86.49%	87.66%
	AA	65.11%	85.59%	85.06%	82.46%

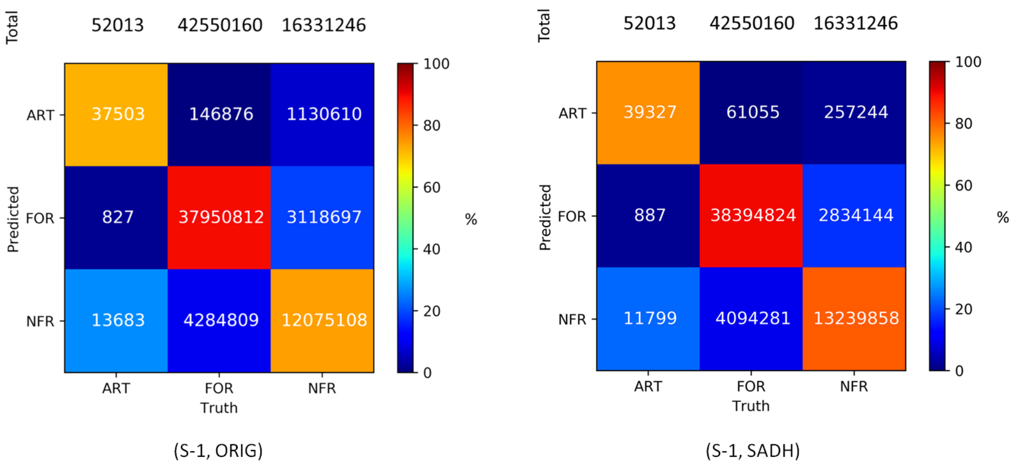

Figure 26: Confusion matrices for the whole test dataset, considering the two analyzed cases, (a) ORIG and (b) SADH. Colors correspond to the normalized number of pixels.

In the following, I consider the Sentinel-1 swath corresponding to stack 7 in Table 4 and provide the performance over a selection of patches. I select four small patches of 512×512 pixels, extending by about 25×25 kilometers on the ground. Referring to Figure 27, patches (a) and (b) are characterized by the presence of urban areas, i.e., the municipalities of Porto Velho and Ariquemes, respectively, while patches (c) and (d) identify stable regions of cropland mixed with remaining rainforest areas.

The results are summarized in Figure 28 and Table 9, which describes the OA and AA for each patch, in both the input configurations, case *(ORIG)* and case *(SADH)*.

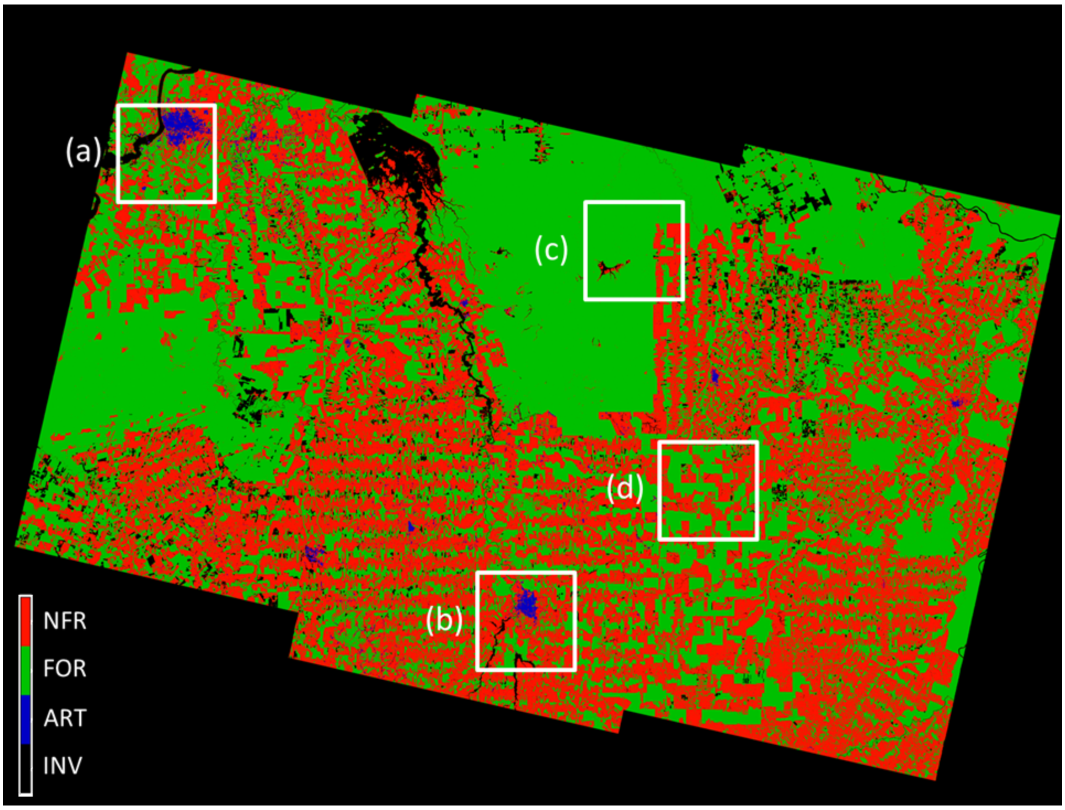

Figure 27: Classification map of the stack number 7 summarized in Tab. 4.

Table 9: Overall accuracy (OA) and Average accuracy (AA) for the four patches in Figure 28. Δ_{OA} and Δ_{AA} represent the increment in (OA) and (AA), respectively, when including textures within the classification.

	class	**patch (a)**	**patch (b)**	**patch (c)**	**patch (d)**
pixels	*ART*	20419	7706	0	0
	FOR	118922	86290	216741	141669
	NFR	100506	155408	42073	117044
case	**metric**	**patch (a)**	**patch (b)**	**patch (c)**	**patch (d)**
ORIG	*OA*	72.31%	80.71%	94.63%	85.88%
	AA	75.94%	79.96%	93.04%	85.79%
SADH	*OA*	73.60%	82.49%	95.75%	87.98%
	AA	78.15%	85.98%	94.28%	87.88%
	Δ_{OA}	1.29%	1.78%	1.12%	2.10%
	Δ_{AA}	2.21%	6.02%	1.24%	2.09%

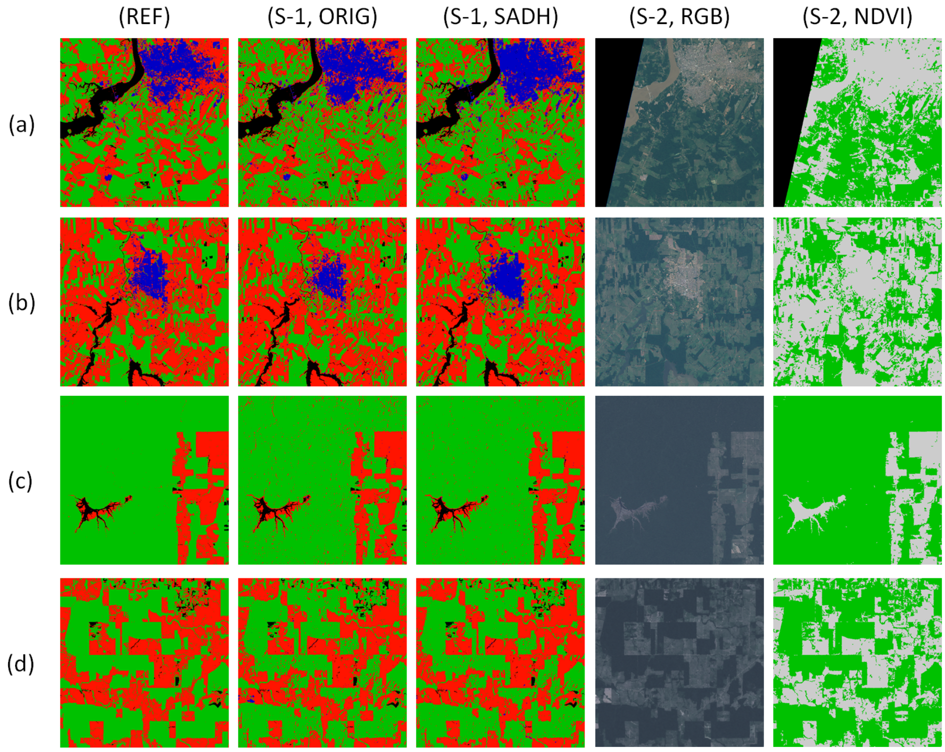

Figure 28: Forest mapping on selected test patches. (REF) modified reference map: FROM-GLC, 2017. (S-1, ORIG) RF classification map using the input parameters from Section 3.2.2. (S-1, SADH) RF result adding the SADH textures to the original parameters. (S-2, RGB) and (S-2, NDVI) optical True Color and NDVI maps of Sentinel-2 acquisitions from the considered month.

By observing the reference (REF) and the results of the case (ORIG) and case (SADH) in Figure 28, it can be seen how the introduction of the texture information in case *(SADH)* helps improve the classification with respect to case *(ORIG)*, by better isolating urban areas and closing gaps over forested areas. The corresponding accuracy values confirm this in Table 9, where a positive increment of both the overall and average accuracy, Δ_{OA} and Δ_{AA}, respectively, is noticed. In particular, in patches (a) and (b), textures are helpful to better classify small details in man-made structures with a consequent increment of accuracy. In patch (c), the inclusion of SADH textures provides a better segmentation of the class *forests* (FOR) with respect to the sole use of interferometric and backscattering parameters. The random noise-like misclassification occurrences are reduced, increasing both OA and AA. Finally, in the patch (d), the introduction of textures also allows for correctly classifying bare soil areas as *non-forested areas* (NFR), which would otherwise result in misclassified *artificial surfaces* (ART).

3.4.3 Monthly deforestation monitoring

In this section, I show and discuss the experimental results obtained by applying the algorithm presented in Section 3.2.4. For the complete analysis I refer to the article in [63]. Table 10 reports the performance of the different Sentinel-1 forest maps, extracted from the time series of May 2019, June 2019, and July 2019, respectively. Figure 29 shows the reference map over footprint 5, used for the performance evaluation: I updated the FROM-GLC map of 2017 with the PRODES polygons (in white) referring to the deforestation that occurred between the 1^{st} of August 2017 and the 31^{st} of July 2019. All forest maps exceed an overall agreement (OA) of 88% and guarantee a well-balance in the classification among the three considered classes, with average accuracies (AA) higher than 83%. Therefore, one can apply the change detection chain presented in Figure 9.

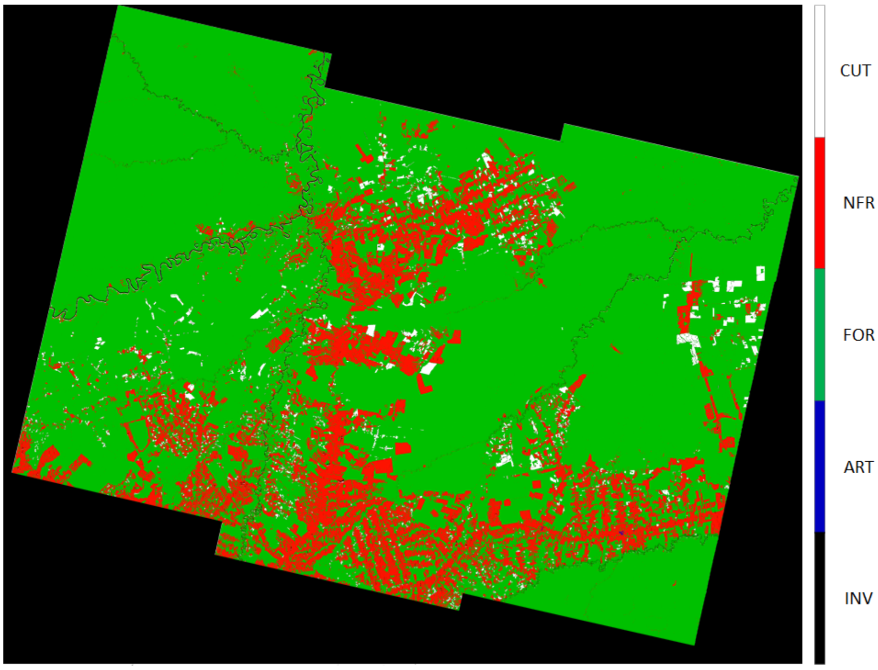

Figure 29: Finer Resolution Observation and Monitoring of Global Land Cover (FROM-GLC, 2017) reference map with in white the clear-cuts (CUT) detected by PRODES between 2017 and 2019. Black: *invalid pixels* (INV), blue: *artificial surfaces* (ART), green: *forests* (FOR), red: *non-forested areas* (NFR), white: *clear-cuts* (CUT).

Figure 30 shows two FROM-GLC maps in grayscale with superimposed colored polygons indicating the detected clear-cuts. The reference map (REF) depicts the annual deforestation hand-marked by PRODES in 2018 (yellow) and 2019 (red). Together, they correspond to the white polygons in Figure 29. The (S-1, DEF) shows in 3 different colored sets of polygons the Sentinel-1 results obtained by processing three different months. The obtained results show great consistency among the polygons detected by the proposed algorithm and those identified by PRODES.

Within the selected test area of footprint 5, I now concentrate on the analysis of three different patches of 1024×1024 pixels size, indicated as (a), (b), (c), and highlighted in blue in Figure

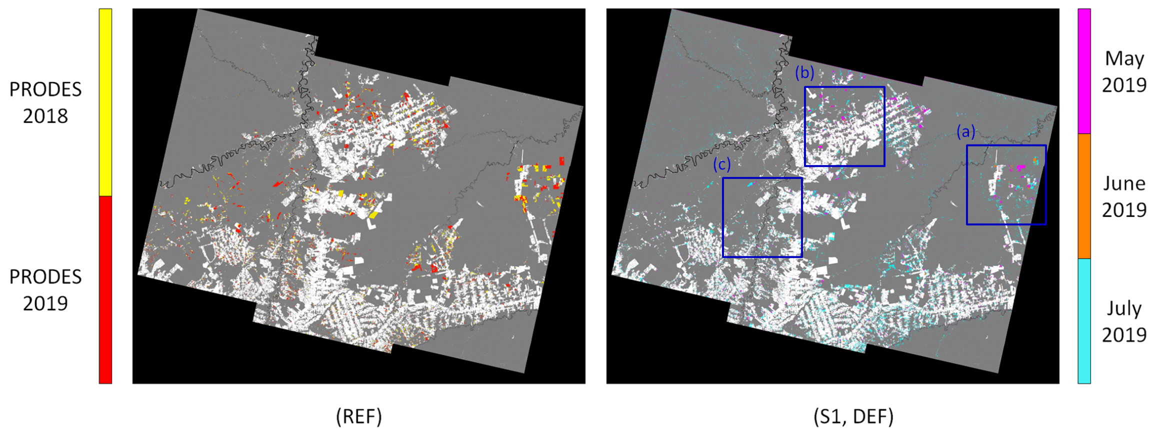

Figure 30: Comparison between the reference map (REF) and the Sentinel-1 deforestation map (S1, DEF).

Table 10: Overall accuracy (OA) and average accuracy (AA) of the forest maps extracted from the three consecutive months over the footprint number 5 in Table 4 and drawn in Figure 29.

Metric	May 2019	June 2019	July 2019
OA	92.82%	91.04%	88.65%
AA	85.21%	83.7%	83.02%

30. In this case, the analysis is carried out by comparing the monthly Sentinel-1 forest map with three vegetation parameters derived from Sentinel-2 acquisitions: the NDVI mask, the NDMI map, and the RGB map, all masked with the invalid pixels of the *Unclassified mask*.

The comparison between the Sentinel-1 forest maps and the Sentinel-2 vegetation parameters for patches (a), (b), and (c) are reported in detail in Figure 31, Figure 32, and Figure 33, respectively.

Figure 31 shows an area affected by deforestation activities taking place in the Summer of 2019. One can identify at least two deforestation hot spots, indicated as (i) and (ii) and delimited by yellow circles in Figure 31. Furthermore, the results show an additional deforestation area located at the bottom of the image, indicated as (iii) in Figure 31. By observing the Sentinel-1 forest map of June 2019, some small-scale activities are visually perceived over the hot spot (iii).

Figure 32 depicts a large plantation area on the eastern side of the municipality of Boca do Acre, state of Amazonas. One can spot some deforestation activities occurring between May 2019 and July 2019 in the left and top-right of the patch. These areas are correctly detected by the Sentinel-1 forest map if compared with the RGB and NDMI from Sentinel-2. In this case, the NDMI index highlights the new cuts as dry pixels, i.e., areas with low water content, not visible within the NDVI image.

Figure 33 presents the southern side of the municipality of Boca do Acre. In this patch, one can identify deforestation activities occurring at the top of the area, marked with a yellow circle.

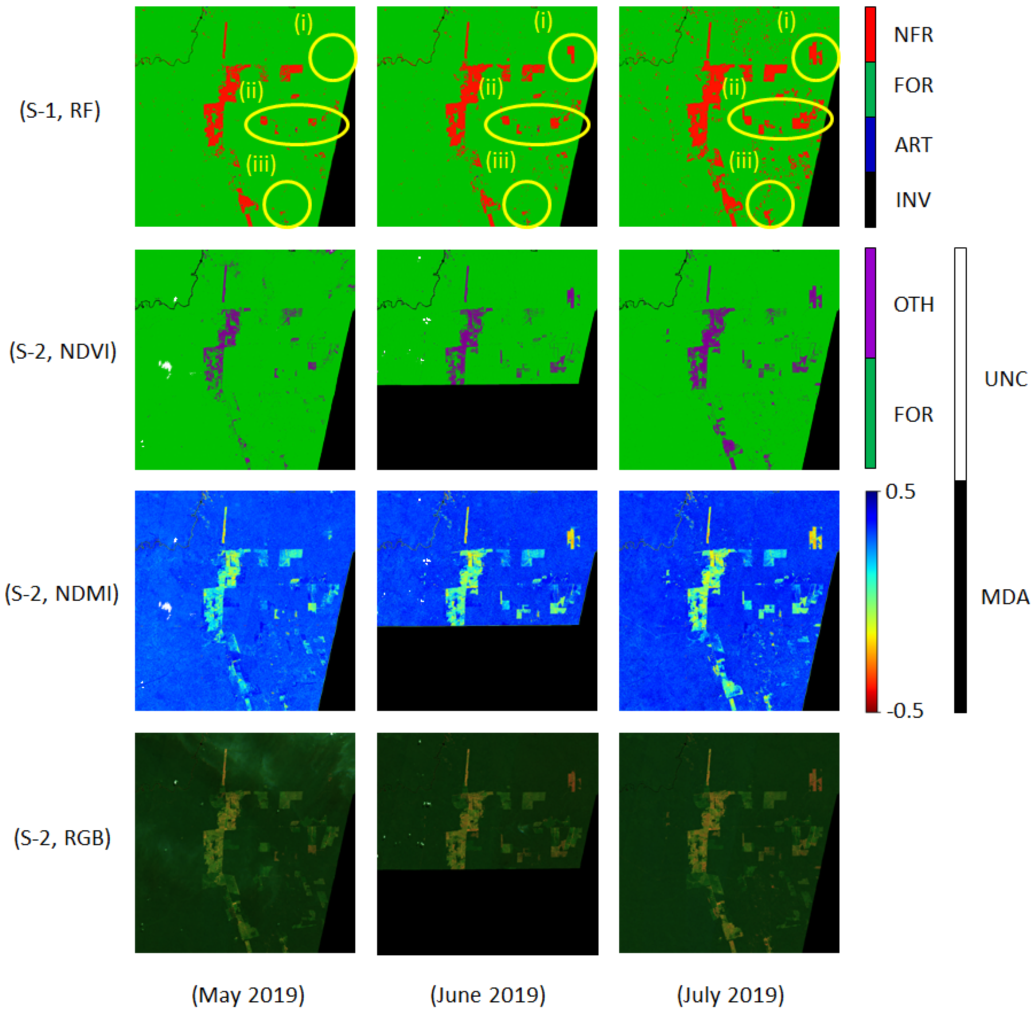

Figure 31: Monthly forest mapping for patch (a). (S-1, RF) Sentinel-1 forest map. (S2, NDVI), (S2, NDMI), and (S2, RGB) Sentinel-2 parameters. The columns indicate the three consecutive months. The yellow circles in (S-1, RF) identify three detected deforestation hot spots, indicated with (i), (ii) and (iii).

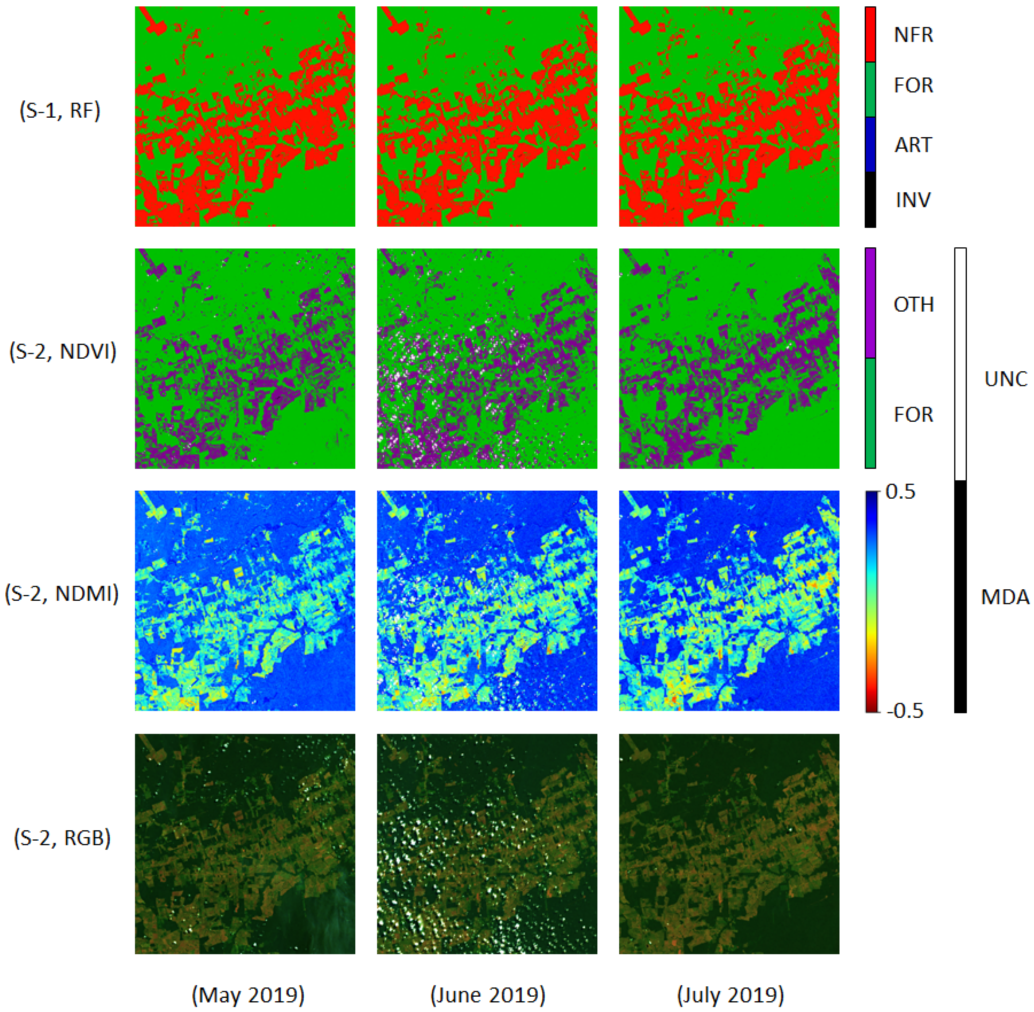

Figure 32: Monthly forest mapping for patch (b) organized as in Figure 31.

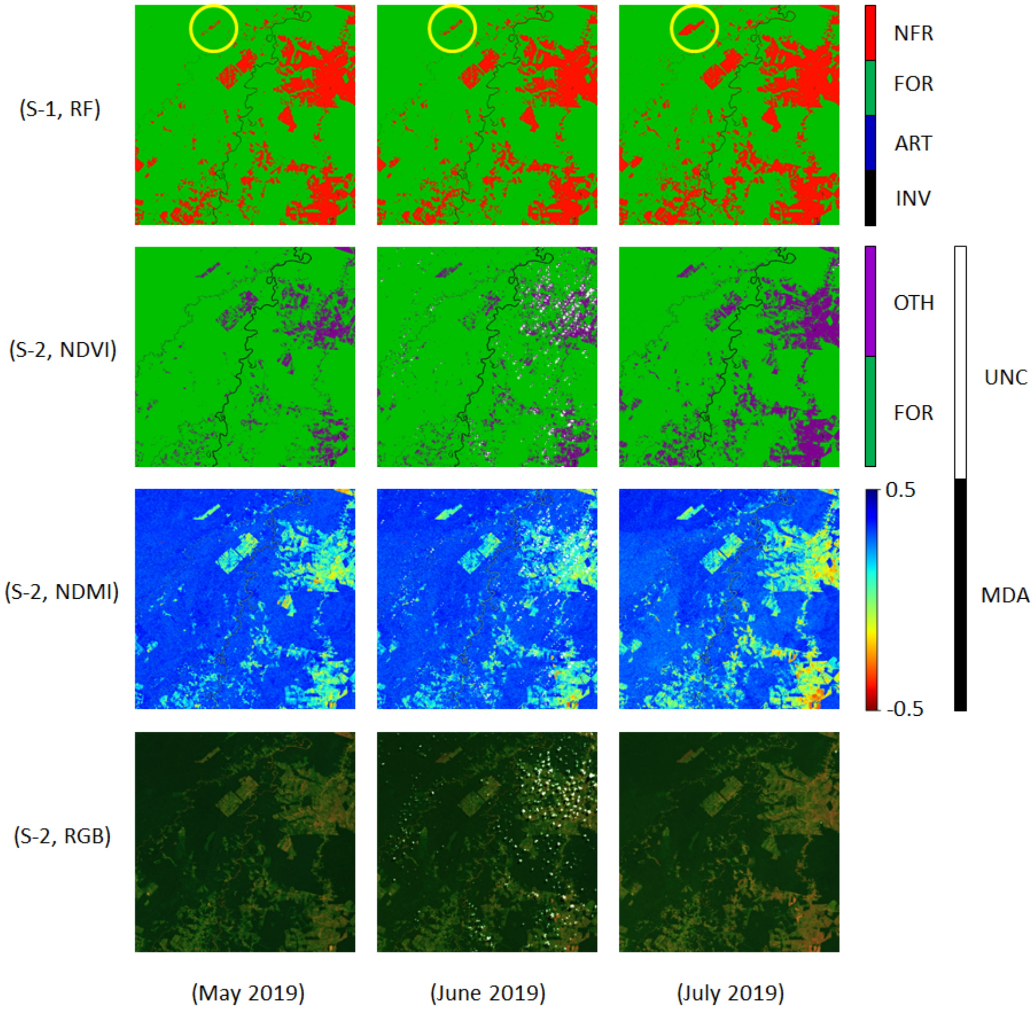

Figure 33: Monthly forest mapping for patch (c) organized as in Figure 31. A deforestation hot spot is detected and indicated with a yellow circle.

The NDVI is here used as a reference mask for evaluating the classification performance of patches (a), (b), and (c) since it represents the best available independent data. Since this mask is binary, the classes *non-forested areas* (NFR) and *artificial surfaces* (ART) are aggregated together in the Sentinel-1 forest maps. I measured the overall accuracy (OA) and, for the forest class (FOR), the precision(P), recall(R), and F1-score (F1). All the numerical results are summarized in Table 11.

The overall accuracy of the Sentinel-1 forest maps consistently exceeds the 80%. As expected, the accuracy values measured for the patch (b) are lower than those computed for the other patches. This behavior is not surprising since the quality of the NDVI mask is much lower for this patch due to cloud cover. Furthermore, one can observe that the classifier can detect the forest class (FOR) with precision consistently higher than 90% and recall not lower than 80%. The F1-Score also shows a similar result, and it consistently exceeds the 86%.

Table 11: Overall accuracy (OA), and, for the FOR class, the precision (P), recall (R), F1-score (F1) of patches (a), (b), and (c).

		May 2019	**June 2019**	**July 2019**
Patch (a)	Date	2019.05.09	2019.06.18	2019.07.08
	OA	96.11 %	94.78 %	93.89 %
	P	98.82 %	98.70 %	99.30 %
	R	97.13 %	95.75 %	94.23 %
	F1	97.97 %	97.20 %	96.70 %
Patch (b)	Date	2019.04.27	2019.06.06	2019.07.01
	OA	83.11 %	81.38 %	84.05 %
	P	96.70 %	93.85 %	97.74 %
	R	80.85 %	80.84 %	80.53 %
	F1	88.07 %	86.86 %	88.30 %
Patch (c)	Date	2019.05.17	2019.06.11	2019.07.11
	OA	87.22 %	86.94 %	89.78 %
	P	98.42 %	98.16 %	97.67 %
	R	87.43 %	87.58 %	89.98 %
	F1	92.60 %	92.57 %	93.66 %

The final results of this work are depicted in the last row of Figure 34, Figure 35, and Figure 36, which show the evolution in time of deforestation activities in patch (a), patch (b), and patch (c). All figures are organized into two rows. The first comprises the references: the FROM-GLC 2017 and the two deforestation masks provided by PRODES in 2018 and 2019. The second row displays the results: the forest maps retrieved on the consecutive months of May, June, and July 2019 and the deforestation maps obtained by applying the processing chain of Figure 9 to the four consecutive forest maps.

Figure 34 shows the polygons retrieved every month by applying the chain presented in Figure 9 on patch (a). According to the results shown in Figure 31, I can draw the following considerations:

- By analyzing patch (a) in May 2019, I can identify a set of polygons, colored from purple to cyan, and highlighted with a white circle, the changes between the FROM-GLC 2017 and the Sentinel-1 forest map generated on that month. The segmentation allows for dividing this cluster of polygons in clear-cuts marked by PRODES in 2018 and 2019. In particular, the cyan polygons, indicated as (i), appear related to activities in 2018, while the bigger one, depicted in purple and marked as (ii), is associated with deforestation recorded in 2019. The purple polygon is a clear-cut created after the 1st of August 2018 but before the end of May 2019. Therefore, the algorithm can increase deforestation maps' temporal resolution by reducing the observation period from one year (as guaranteed by PRODES) to one month.
- Some areas in the bottom-left of the image are classified in PRODES 2018 as clear-cuts, while the algorithm recognized some of them only in July 2019. The Sentinel-2 images of vegetation parameters in Figure 31 confirm the accuracy of the results.
- On the upper-right corner of the image, one can observe the evolution of a clear-cut,

firstly detected in June 2019, that expanded towards the east during July 2019. This cut is registered on the PRODES 2019 map only according to the references.

- On the right side of the image, one can identify a deforestation activity starting after June 2019 and correctly detected in PRODES 2019.

Figure 35 reports the results of the monthly deforestation over patch (b). As expected, more changes are detected during May 2019. By comparing the results of May 2019 with the two deforestation maps of PRODES, one can observe that: those polygons in blue (i), light green (ii), dark green (iii) are marked by PRODES analysts in the year 2018, while the remaining four clusters (white (iv), orange (v), yellow (vi) and purple (vii)) are identified in 2019. From May to July 2019, small-scale deforestation activities are detected. This result can also be explained by the fact that plantations mostly dominate the area under test, as shown in the Sentinel-2 RGB maps of Figure 32.

Finally, Figure 36 presents the results of the monthly deforestation over patch (c). According to PRODES maps, this area is not particularly involved in deforestation activities. One can observe two main aspects:

- On the upper side of the image, deforestation activities were detected by PRODES in 2019. Our result suggests that the activity over this area is mainly occurring during July 2019. However, the algorithm detects a little polygon in May 2019, which is confirmed by the Sentinel-1 forest map and Sentinel-2 parameters of Figure 33.

- Some other discrepancies between the results and the PRODES reference are noticed. The PRODES deforestation maps of 2018 and 2019 identify an area of deforestation activities in the middle of the image. By observing Figure 33, though, I can assume that this is a problem of sensor sensitivity since neither the Sentinel-2 NDVI index nor the Sentinel-2 NDMI one recognizes this hotspot.

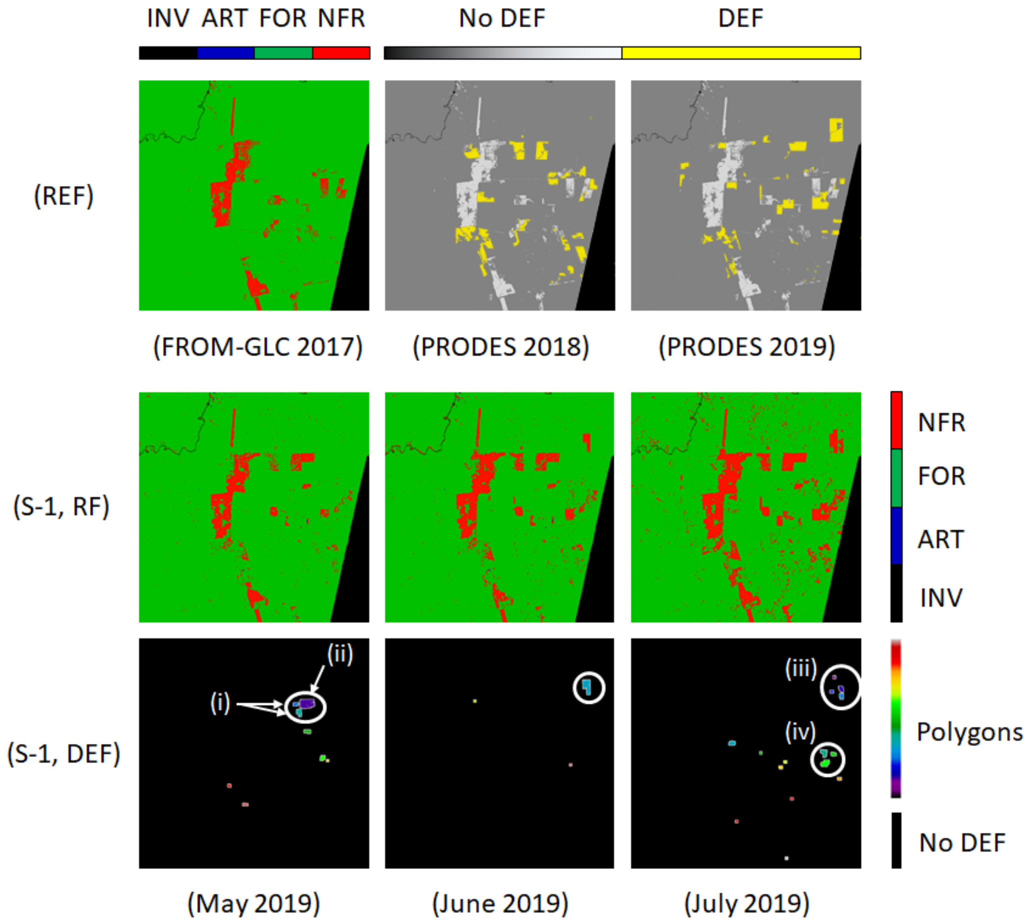

Figure 34: Monthly deforestation monitoring for patch (a). (REF) three used references FROM-GLC 2017 and PRODES deforestation (yellow) of 2018 and 2019. (S-1, RF) Sentinel-1 monthly forest maps. (S-1, DEF) Sentinel-1 monthly deforestation map.

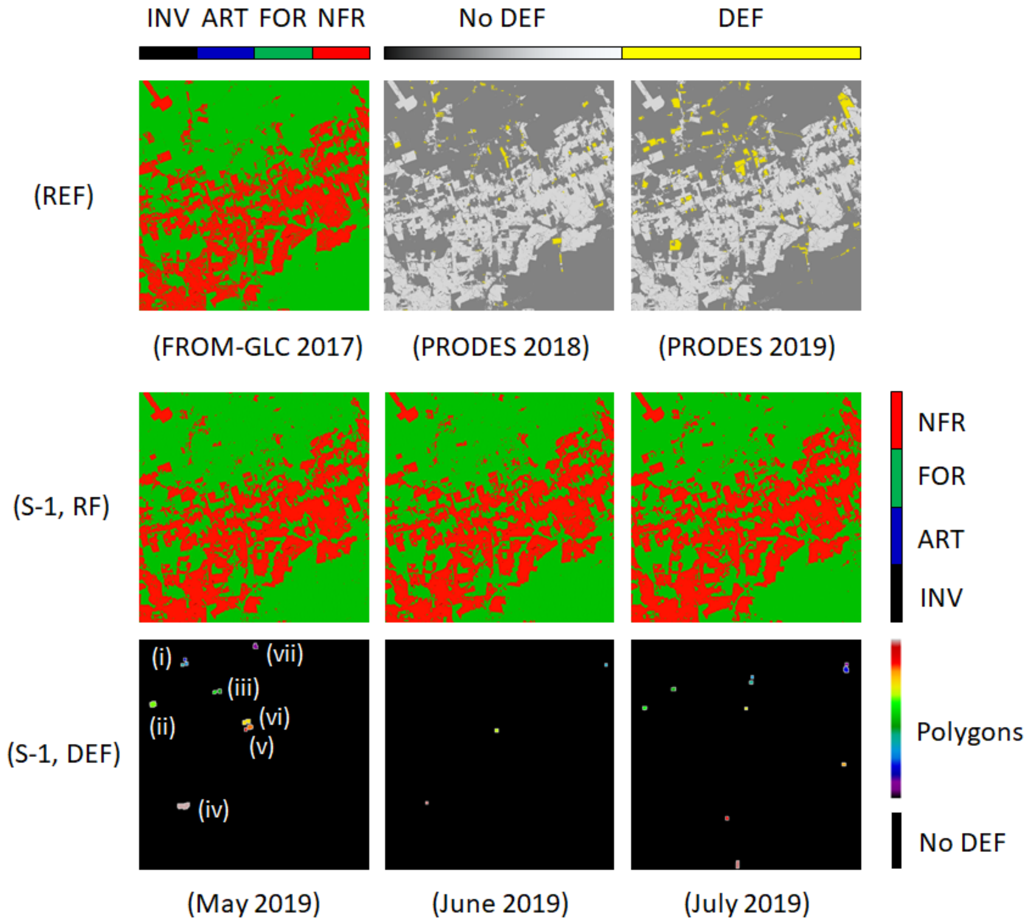

Figure 35: Monthly deforestation monitoring for patch (b). (REF) three used references FROM-GLC 2017 and PRODES deforestation (yellow) of 2018 and 2019. (S-1, RF) Sentinel-1 monthly forest maps. (S-1, DEF) Sentinel-1 monthly deforestation map.

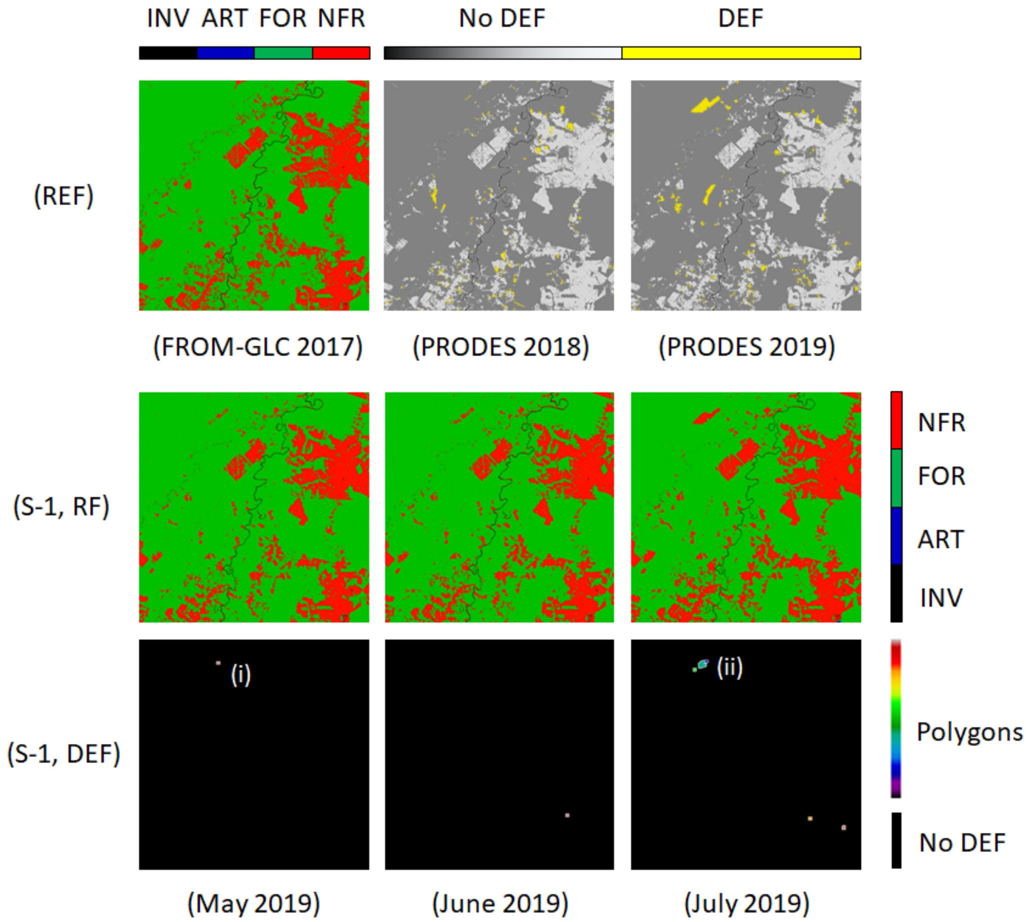

Figure 36: Monthly deforestation monitoring for patch (c). (REF) three used references FROM-GLC 2017 and PRODES deforestation (yellow) of 2018 and 2019. (S-1, RF) Sentinel-1 monthly forest maps. (S-1, DEF) Sentinel-1 monthly deforestation map.

3.4.4 Temporal decorrelation analysis at X band

In this section, I report the analysis on temporal decorrelation at X band, introduced in Section 3.2.1. For all considered land cover classes, I first fitted the ρ_{vol} trends as a function of h_{amb} from archived TDM acquisitions, by fitting the exponential model in eq.(3.7). The results are shown in Figure 37 and the fitting parameters, together with the fitting root mean square error (RMSE), are summarized in Table 12.

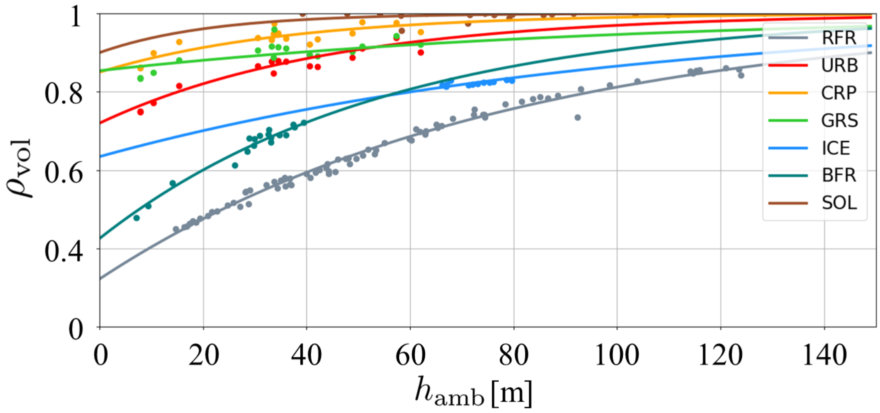

Figure 37: Exponential fittings of ρ_{vol} as a function of h_{amb} for all the considered land cover classes.

I show the fitted ρ_{temp} trends in Figure 38 for each considered land cover class:

- URB: *Urban areas*
- SOL: *Soil and rocks*
- ICE: *Snow and ice*
- CRP: *Crops*
- GRS: *Grasses*
- RFR: *Rainforest*
- BRF: *Boreal forest*

The results are split into two different subplots where the corresponding ρ_{tot} (triangle symbol), η (cross symbol), and ρ_{temp} (dot symbol) per image are depicted. The plots are grouped as follows. The first plot shows the results for the *Urban areas* (URB), *Soil and rocks* (SOL), and *Snow and ice* (ICE). The first two classes are typically the most stable in time and are characterized by high temporal coherence. Regarding *Snow and ice*, the selected test site is located in the inner part of the Greenland plateau, which is characterized by the presence of dry snow (no melting phenomena are present) and shows, therefore, a relatively high temporal coherence. Moreover, over dry snow, radar waves at the X band penetrate the snowpack and are gradually absorbed with increasing depth, while only a fraction is backscattered toward

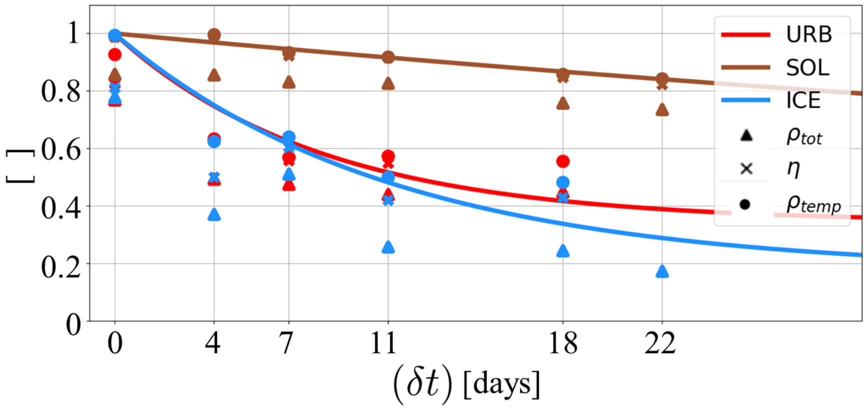

(a)

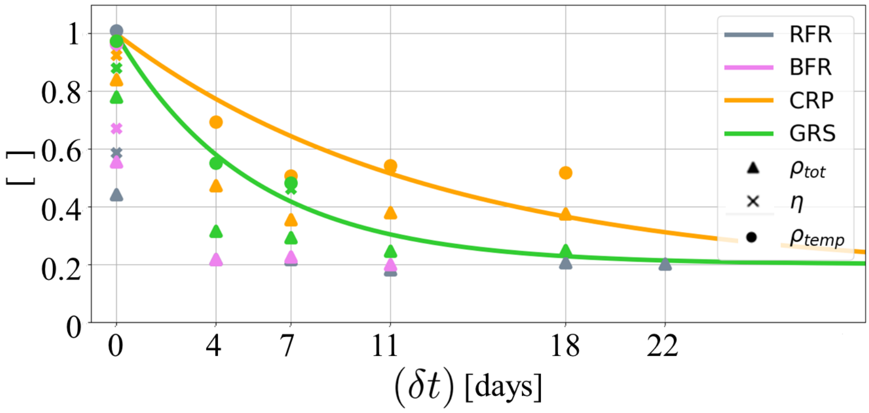

(b)

Figure 38: Mean ρ_{tot}, η, and ρ_{temp} with respect to the temporal baseline δt for all the considered land cover classes. The continuous lines identify the corresponding exponential fittings of ρ_{temp}.

the radar platform. Therefore, a significant volume decorrelation takes place as well, as clearly visible in Figure 37.

The second plot groups together all classes characterized by the presence of different sort of vegetation: *Crops* (CRP), *Grasses* (GRS), *Rainforest* (RFR), and *Boreal forest* (BFR). In particular, *Crops* and *Grasses* identify areas characterized by the presence of low vegetation. They can show a certain variability depending on the seasonality, while *Rainforest* and *Boreal forest* correspond to two different kinds of forests. The first type is typically characterized by a tree density that is higher than the second one, and both classes show significant volume decorrelation phenomena, as observed in Figure 37. This behavior is normally caused by multiple scattering from the canopies, trunks, branches, and, in the presence of significant gaps, from the ground itself.

From the plots in Figure 38 and the RMSE values listed in Table 12, I observe how the compensation of ρ_{vol} leads to a better interpretation of the temporal behavior of the imaged target. Indeed, when applying the same fitting procedure to $\eta(\delta t)$, it systematically shows a higher RMSE with respect to the $\rho_{\text{temp}}(\delta t)$. As expected, the most stable land cover classes, *Soil and rocks* and *Urban areas* at Figure 38 (a), maintain higher levels of coherence even at larger temporal baselines. Considering the Greenland test site in the same subplot, one can notice how the targets almost completely decorrelate for circa $\delta t = 30$ days and show an overall trend similar to the urban case one. Additional data show that ρ_{temp} has reached the bias for $\delta t = 44$ days. I omit this result in Figure 38 for the sake of the plot's clarity. Of course, it has to be pointed out that this case cannot generalize the behavior of all snow-covered regions. On the contrary, only Greenland or Antarctica presents large dry snow areas. All other snow- and ice-covered areas are typically affected by significant melting phenomena that can change the structure of the snow and, therefore, strongly impact the temporal coherence decay.

Crops and *Grasses*, depicted in Figure 38 (b), decorrelate much faster than pure *Soil and rocks*. For example, it is caused by seasonal vegetation on the ground, changing soil moisture, and harvesting activities. In the specific analysis, all available InSAR pairs were acquired during September 2019, so it is reasonable to assume substantial stability of the illuminated scene. Moreover, one can notice that I did not fit any exponential model to both *Rainforest* and *Boreal forest* classes. Such land cover classes completely decorrelate after a δt, shorter than the minimum available revisit time of 4 days. Indeed, I recorded stable values of ρ_{tot} around 0.2, independently from the considered δt and h_{amb}. For this reason, an exponential fitting of the temporal decay is not meaningful. The ρ_{temp} fitting parameters for all the available land cover classes, forests excluded, and the corresponding RMSE are summarized in Table 12.

Table 12: $\rho_{\text{vol}}(h_{\text{amb}})$, $\rho_{\text{temp}}(\delta t)$, and $\eta(\delta t)$ fitting coefficients. Note that the $\hat{\rho}_{\text{LT}}$ is reported once since it is the same for both temporal decorrelation fittings.

Fitting coefficients and RMSE								
	$\rho_{\text{vol}}(h_{\text{amb}})$			$\rho_{\text{temp}}(\delta t)$			$\eta(\delta t)$	
Land Cover	$\hat{\alpha}$	$\hat{\beta}$	RMSE	$\hat{\rho}_{\text{LT}}$	$\hat{\tau}$	RMSE	$\hat{\tau}$	RMSE
Soil and rocks	0.1	21.4173	0.0111	0.2007	103.9013	0.0125	93.4605	0.0132
Urban areas	0.28	45.0512	0.04	0.3429	8.2674	0.0661	7.7617	0.0826
Crops	0.1499	36.8656	0.0253	0.1658	12.6259	0.0779	12.4581	0.0781
Grasses	0.1461	100.01	0.0315	0.1656	5.3829	0.0326	4.8687	0.0521
Rainforest	0.6777	77.9722	0.0128	-	-	-	-	-
Boreal forest	0.5743	55.1436	0.0335	-	-	-	-	-
Snow and ice	0.3655	100.3	0.0054	0.1730	11.1726	0.0757	8.6408	0.1077

3.4.5 Deep Learning semantic segmentation

In the following, I present the results obtained by using the methodology presented in 3.2.5. The presented network takes as input the multi-temporal backscatter γ^0, the incidence angle θ_{inc}, the decorrelation constant τ, and the long-term coherence ρ_{LT}. The model is trained over 20 epochs as depicted in Figure 39, which shows the evolution of training and validation loss.

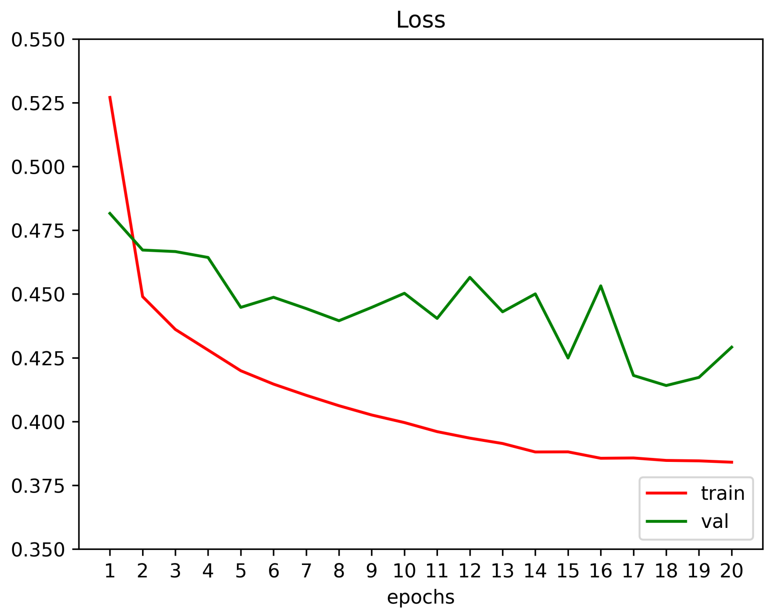

Figure 39: Training and validation loss evolution with increasing epoch number.

To assess the methodology performance, I compare with the same reference used for forest mapping and introduced in Section 3.3.2. As a baseline algorithm, I select the RF one presented in Section 3.2.3. Both models are trained under the same conditions, such as input parameters and number of samples. The output map is a binary mask localizing forested areas. I consider two test images 1000×1000 pixels large and assess the performance through the overall accuracy and F1-score. Figure 40 and Figure 41 show the two test site.

From a first visual inspection, one can notice that the DL approach guarantees a much more homogeneous map and reduces granular noise in the result. Still, some areas differ from the reference for the RF classifier. Since both algorithms behave the same in those areas, it is convincing that very probably, as already shown in Section 3.4.2 that the reference is not up to date. Specifically, from Figure 40 related to test case 1, one can notice that the U-Net allows for a much more stable behavior, especially in areas with varying topography (upper part of the image), while preserving the edges of the non-forested areas. Similarly, test case 2 in Figure 41 shows that the U-Net can much better follow the forest contour.

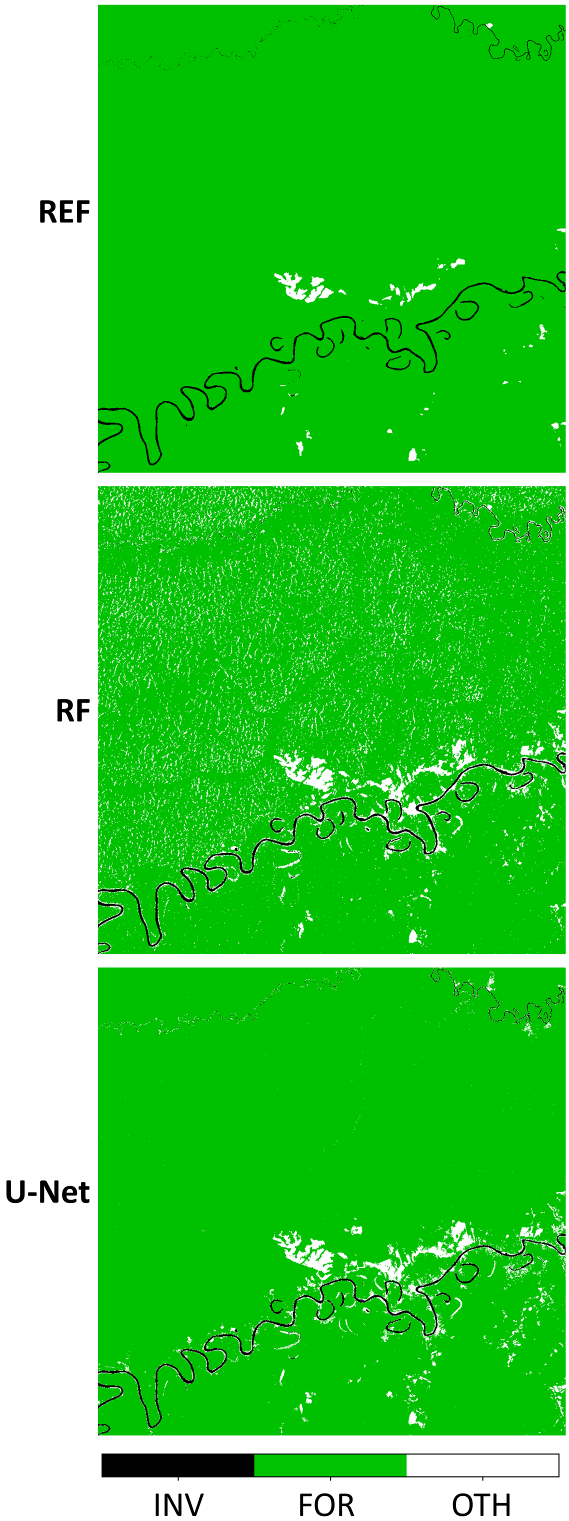

Figure 40: Comparison between the reference map (REF), the proposed U-Net model, and the RF classifier for test case 1.

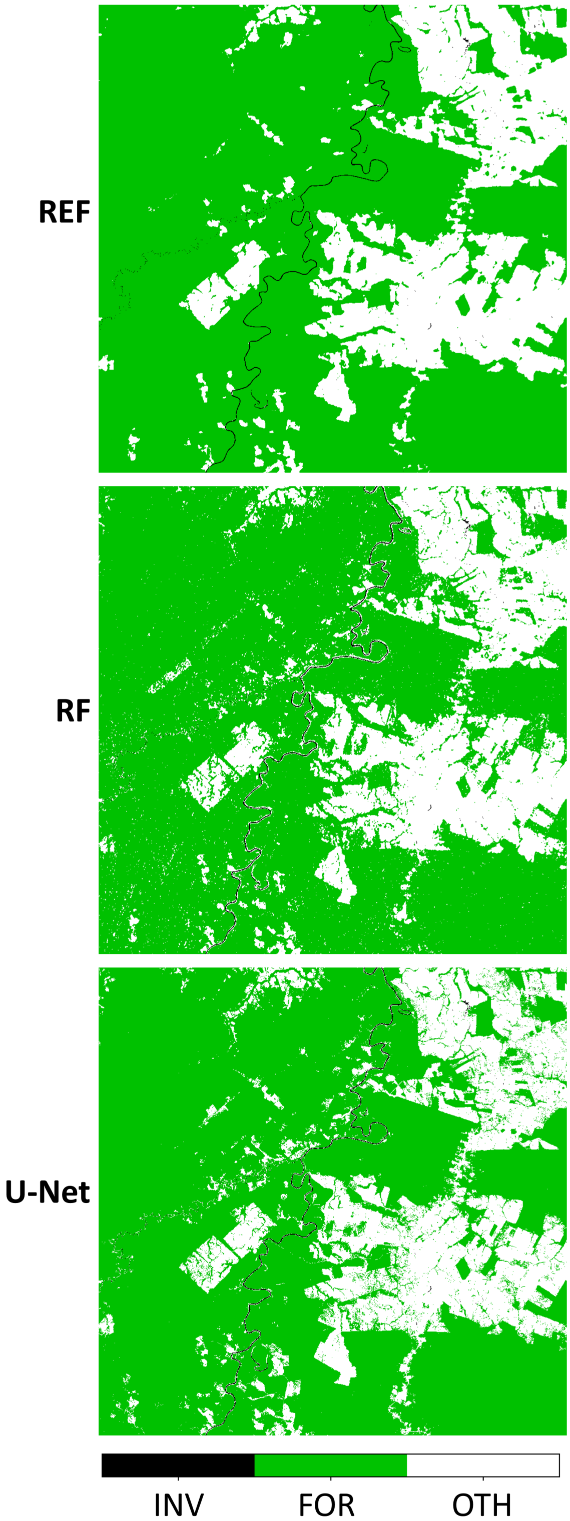

Figure 41: Comparison between the reference map (REF), the proposed U-Net model, and the RF classifier for test case 2.

These observations are further confirmed by the numerical results depicted in Table 13 and Table 14. In all cases, the DL approach improves the overall accuracy and F1-score result.

Table 13: Overall accuracy (OA) and F1-score (F1) of the forest maps generated with the RF and the proposed U-Net model for test case 1.

Metric	RF	U-Net
OA	93.04%	97.51%
F1	96.33%	98.73%

Table 14: Overall accuracy (OA) and F1-score (F1) of the forest maps generated with the RF and the proposed U-Net model for test case 1.

Metric	RF	U-Net
OA	92.12%	94.73%
F1	93.63%	95.75%

By comparing these results with the one obtained with the methodology presented in Section 3.2.3, one can observe that the use of the U-Net brings improvements that are similar to the one obtained by considering the texture parameters in the RF algorithm. This behavior can be explained intuitively by highlighting that convolutional neural networks intrinsically perform a spatial analysis by internally generating from low-level to high-level features extracted from the input images. Therefore one can conclude that the use of DL approaches can be beneficial for this purpose.

4. Conclusions and recommendations

In the presented research project, I investigated methodologies to infer land cover and land use classes from interferometric time series using novel ML approaches. The HI-FIVE project - High-Resolution Forest Coverage with InSAR & Deforestation Surveillance - targeted forest mapping and deforestation monitoring. Nevertheless, the research investigation has been conducted in very general terms to classify different land cover/use classes. I focused on exploiting the Sentinel-1 time series and, specifically, its interferometric capability. Likewise, I had the opportunity to investigate different ML approaches, from the well-established Random Forests classifier, to more recent DL approaches.

From the presented results, one can claim that repeat-pass InSAR is a precious tool for land cover/land use classification. The proposed methodologies have been tested at different aims. First, a general framework for land cover classification has been proposed and tested with a dataset covering Europe. This investigation set the groundwork for adequately exploiting coherence time-series at different temporal baselines. Secondly, this approach has been used to map forested areas and applied to the Amazon rainforest test case. Additional features have been considered to improve the classification, such as texture features. Eventually, a framework for the monthly deforestation monitoring has been proposed and tested over the Amazon rainforest, where the most intense deforestation phenomena currently occur. The whole research investigation has been supplied with additional side-studies, such as the analysis of temporal decorrelation at X band and the use of DL models to improve the end-product spatial and temporal resolution.

Wrapping up the project findings, I can affirm that interferometric parameters are crucial for land cover/use classification. It is especially true when a more significant number of inferred classes is targeted. The exclusive use of the backscatter or the interferometric parameters for land cover leads to similar overall performance. For the *forests* class, so as for the *artificial surfaces* one, the interferometric parameters show better classification performance. Nevertheless, the use of the interferometric parameters $\hat{\tau}$ and $\hat{\rho}_{\mathrm{LT}}$ represents a piece of valuable additional information with respect to the multi-temporal backscatter $\hat{\gamma}^0$. When applying the algorithm to forest mapping, the use of backscatter spatial textures significantly improves the correct discrimination between *non-forested areas* and *artificial surfaces*. The results obtained over an area belonging to the Rondonia State, Brazil, achieved an overall accuracy above 80%. The proposed forest mapping methodology has set the basis for developing an operational framework for effectively monitoring forest changes at a monthly rate. This last aspect is of great interest for developing an early-warning system, which could effectively support the deputy authorities in identifying illegal deforestation hot-spots and, therefore, protect the rainforest resources. By performing change detection between subsequent multi-temporal stacks, the methodology developed in this project can monitor deforestation activity on a monthly scale. The experiments reported in this paper confirm the high potential of multi-temporal interferometric time series for forest mapping and deforestation monitoring. Indeed, by systematically iterating the proposed processing chain, a change detection algorithm can be applied by comparing the forest map results from subsequent multi-temporal stacks. The newly provided result obtained by the presented change detection methodology of Section 3.2.4 provides additional value to the already available change maps by improving end-product accuracy and temporal resolution.

The research investigation pointed out possible sources of uncertainty coming from the three reference maps considered in the analysis and could be the object of future investigations:

- The FROM-GLC map is older than the exploited Sentinel-1 time series, causing a mismatch due to temporal changes. Furthermore, this map is more sensitive to sparse vegetation with respect to Sentinel-1, minimizing the areas covered by bare soil and rocky surfaces.
- The PRODES map has a lower temporal and spatial resolution. New clear-cuts are provided once per year. Due to possible human errors and a minimum mapping area of 6,25 hectares, the map accuracy is reduced.
- The S-2 NDVI map is impaired from cloud coverage, which is common in areas like the Amazon rainforest. Therefore, it cannot guarantee temporal and spatial continuity.

I additionally performed side-investigations within this project. One of these is the analysis of decorrelation phenomena at the X band by exploiting the TDM-PAZ constellation. I separated volume and temporal decorrelation components for different land cover classes and analyzed their behavior over five test sites. The proposed methodology has been proved by exploiting all the TDM-PAZ time series that were available at the time of the analysis. The results highlighted different behaviors at C and X bands. Indeed, no analysis on the forest class is possible at X band, whose data reach the maximum decorrelation already after four days. Differently, the behavior of other classes reflects the analysis findings on Sentinel-1 data. Furthermore, the proposed work highlighted the importance of combined bistatic and repeat-pass systems in view of future SAR constellations designed to monitor Earth's dynamics. It is worth mentioning that this kind of analysis on temporal decorrelation can be a valuable input for missions design, e.g., selecting appropriate revisit time and assessing the interferometric performance.

Eventually, DL approaches have been investigated. The Φ-Net has been beneficial to spatial resolution for forest mapping purposes. An example of a coherence map has been provided. This methodology can achieve an unprecedented trade-off between estimation accuracy and resolution preservation. In addition to that, the temporal resolution has been further addressed with DL-based semantic segmentation. The U-Net model can be exploited to perform single coherence image classification and reduce deforestation monitoring to a 6 (or 12) day scale. Though the investigation needs to be completed, the first obtained results using temporal decorrelation parameters encourage and justify additional investigations.

Given the obtained results, my recommendations for future research concern the investigation of similar methodologies to increase the number of input and output parameters and improve the interferometric parameters' estimation. The former may concern different input features, such as polarimetric SAR (PolSAR) parameters and an increased number of inferred classes. The latter may aim to improve the estimation of the temporal interferometric parameters after temporal decorrelation retrieval in place of the already proposed least-square optimization problem.

Additionally, one can find a way to consider seasonal variations by taking into account:

- monthly scale maps: needs to recognize the season to increase the robustness of the algorithm;

- yearly scale mapping: seasonality can itself bring information about the class, e.g., it is expected to observe a seasonal variability for *non-forested areas* with respect to *artificial surfaces* classes.

Eventually, DL methodologies can be further developed. While the interferometric phase and coherence estimation have already been largely investigated in this project, semantic segmentation could still be improved. Indeed, it will be needed to assess the best classification accuracy among input parameters, network model, and classification strategy. Alternatively, one could use a DL approach to classify the single coherence map and generate forest maps every six days or perform change detection by directly processing coherence time series.

5. Publications

Journal papers

1. Sica, F., Bretzke, S., Pulella, A., Bueso-Bello, J. L., Martone, M., Prats-Iraola, P., González-Bonilla, M. J., Schmitt, M., Rizzoli, P. (2020). *InSAR decorrelation at X-band from the joint TanDEM-X/PAZ constellation.* IEEE Geoscience and Remote Sensing Letters.

2. Pulella, A., Sica, F., Rizzoli, P. (2020). *Monthly Deforestation Monitoring with Sentinel-1 Multi-temporal Signatures and InSAR Coherences.* Revista de Teledetección, (56), 1-22.

3. Sica, F., Gobbi, G., Rizzoli, P., Bruzzone, L. (2020). Φ*-Net: Deep Residual Learning for InSAR Parameters Estimation.* IEEE Transactions on Geoscience and Remote Sensing, 59(5), 3917-3941.

4. Pulella, A., Aragão Santos, R., Sica, F., Posovszky, P., Rizzoli, P. (2020). *Multi-temporal sentinel-1 backscatter and coherence for rainforest mapping.* Remote Sensing, 12(5), 847.

5. Sica, F., Pulella, A., Nannini, M., Pinheiro, M., Rizzoli, P. (2019). *Repeat-pass SAR interferometry for land cover classification: A methodology using Sentinel-1 Short-Time-Series.* Remote Sensing of Environment, 232, 111277.

Selected conference papers

1. Bueso-Bello, J. L., Pulella, A., Sica, F., Rizzoli, P. (2021, July). *Deep Learning for Mapping the Amazon Rainforest with TanDEM-X.* In 2021 IEEE International Geoscience and Remote Sensing Symposium IGARSS (pp. 1549-1552). IEEE

2. Pulella, A., Sica, F., Rizzoli, P. (2021, March). *Amazon Rainforest Mapping using Sentinel-1 Short Time Series.* In EUSAR 2021; 13th European Conference on Synthetic Aperture Radar (pp. 1-4). VDE.

3. Sica, F., Pulella, A., Rizzoli, P. (2019, July). *Forest Classification and Deforestation Mapping by Means of Sentinel-1 InSAR Stacks.* In IGARSS 2019-2019 IEEE International Geoscience and Remote Sensing Symposium (pp. 2635-2638). IEEE.

4. Bueso Bello, J. L., Rizzoli, P., Sica, F. (2019). *Estimating the Deforestation Rate in the Amazon Rainforest from Sentinel-1 and TanDEM-X Multi-Temporal Stacks.* In International Geoscience and Remote Sensing Symposium (IGARSS). ESA.

6. Acknowledgments

In conclusion of this project report, I could not forget mentioning the people and institutions that made the project possible in the first place and that actively contributed to its success. It has been a long way, and I could carry out my work with enthusiasm thanks to the support of ESA's staff members. I am incredibly grateful to my ESA supervisor, Dr. Frank Martin Seifert, who helped me steer my research investigation and facilitate contact with Brazilian stakeholders interested in applying my findings to their case studies. I would also like to thank Dr. Anca Anghelea and Dr. Diego Fernández Prieto for coordinating the ESA Living Planet Fellowship's activities, assisting with suggestions, and putting additional resources at my disposal for the successful fulfillment of my research investigation. I want to express my deepest thanks to Dr. Henri Laur, Dr. Pierre Potin, and Luca Martino for the fruitful discussions about the Sentinel-1 acquisition scenarios and further planning of Sentinel-1 acquisitions over the Amazon rainforest. I also wish to thank María José González Bonilla of the National Institute for Aerospace Technology (INTA), which provided PAZ data for an unprecedented analysis on the combined use of data from TanDEM-X and PAZ mission. I want to pay my special regards to Dr. Gianfranco Fornaro and Prof. Ralph Dubaya for believing and recommending my project to ESA during the selection process. Their vital contribution has let me accomplish this great opportunity. This project would not have been possible without the support of Prof. Alberto Moreira and the Microwaves and Radar Institute of the German Aerospace Center, which he is leading. I had the opportunity to capitalize on the Institute's long-standing experience in Synthetic Aperture Radar and create novel methodologies by building on the Institute's knowledge. Last but not least, I thank my friend and colleague Andrea Pulella, who shared joyful and challenging work moments with me, which increased our motivation and satisfaction to keep working hard in the beautiful field of Remote Sensing.

Bibliography

[1] ESA. Copernicus: Sentinel-1 — The SAR Imaging Constellation for Land and Ocean Services. https://directory.eoportal.org/web/eoportal/satellite-missions/c-missions/copernicus-sentinel-1, Nov. 2018. [Online]. accessed 13.01.2022. 11

[2] DLR. TanDEM-X - the Earth in three dimensions. https://www.dlr.de/content/en/missions/tandem-x.html. [Online]. accessed 13.01.2022. 11

[3] Hisdesat. The PAZ Mission. https://www.hisdesat.es/en/paz/, Apr. 2020. [Online]. accessed 13.01.2022. 11, 18

[4] F. Sica, D. Reale, G. Poggi, L. Verdoliva, and G. Fornaro. Nonlocal adaptive multilooking in SAR multipass differential interferometry. *IEEE Journal of Selected Topics in Applied Earth Observations and Remote Sensing*, 8(4):1727–1742, 2015. 12

[5] M. Sarker, J. Nichol, H. Iz, B. B. Ahmad, and A. Rahman. Forest Biomass Estimation Using Texture Measurements of High-Resolution Dual-Polarization C-Band SAR Data. *IEEE Transactions on Geoscience and Remote Sensing*, 51:3371–3384, 2013. 12

[6] F. Sica, G. Gobbi, P. Rizzoli, and L. Bruzzone. Φ-Net: Deep Residual Learning for InSAR Parameters Estimation. *IEEE Transactions on Geoscience and Remote Sensing*, 59(5):3917–3941, 2020. 13, 32

[7] M. C. Hansen, P. V. Potapov, R. Moore, M. Hancher, S. A. Turubanova, A. Tyukavina, D. Thau, S. V. Stehamn, S. J. Goetz, T. R. Loveland, and J. R. G. Kommareddy. High-resolution global maps of 21st century forest coverage change. *Science*, 342:850–853, Nov. 2013. 15

[8] R. O. Dubayah and J. B. Drake. Lidar remote sensing for forestry. *Journal of Forestry*, 98(6):44–46, Jun. 2000. 15

[9] B. Mora, N. E. Tsendbazar, M. Herold, and O. Arino. Global Land Cover Mapping: Current Status and Future Trends. In I. Manakos and M. Braun, editors, *Land Use and Land Cover Mapping in Europe. Remote Sensing and Digital Image Processing*, volume 18, chapter 2. Springer, 2014. 15

[10] C. Schmullius, C. Thiel, C. Pathe, and M. Herold V. Avitabile. DUE GlobBiomass-Estimates of Biomass on a Global Scale. *AGU Fall meetings abstract*, 2016. 15

[11] S. Hese, W. Lucht, C. Schmullius, M. Barnsley, R. Dubayah, D. Knorr, K. Neumann, T. Riedel, and K. Schrüter. Global biomass mapping for an improved understanding of the CO2 balance — the Earth observation mission Carbon-3D. *Remote Sensing of Environment*, 94:94–104, 2005. 15

[12] M. C. Dobson, F. T. Ulaby, and L. E. Pierce. Land-cover classification and estimation of terrain attributes using synthetic aperture radar. *Remote Sensing of Environment*, 51(1):199–214, Jan. 1995. 15

[13] Z. Malenovsky, H. Rott, J. Cihlar, M. E. Schaepman, G. Garcia-Santos, R. Fernandes, and M. Berger. Sentinels for science: Potential of Sentinel-1,-2, and-3 missions for scientific observations of ocean, cryosphere, and land. *Remote Sensing of Environment*, 120:91–101, 2012. 15

[14] M. Ruetschi, M. E. Schaepman, and D. Small. Using Multitemporal Sentinel-1 C-band Backscatter to Monitor Phenology and Classify Deciduous and Coniferous Forests in Northern Switzerland. *Remote Sensing*, 10(1):1–30, Jan. 2018. 15

[15] M. Shimada, T. Itoh, T. Motooka, M. Watanabe, T. Shiraishi, R. Thapa, and R. Lucas. New global forest/non-forest maps from ALOS PALSAR data (2007-2010). *Remote Sensing of Environment*, 155:13–31, 2014. 15

[16] A. Luckman, J. Backer, T. Mora Kuplich, C. da Costa Freitas, and A. C. Frery. A study of the relationship between radar backscatter and regenerating tropical forest biomass for spaceborne SAR instrument. *Remote Sensing of Environment*, 60:1–13, 1997. 15

[17] M. Santoro, C. Beer, O. Cartus, C. Schmullius, A. Shvidenko, I. I. McCallum, and A. Wiesmann. Retrieval of growing stock volume in boreal forest using hyper-temporal series of Envisat ASAR ScanSAR backscatter measurements. *Remote Sensing of Environment*, 115(2):490–507, 2011. 15

[18] O. Cartus, M. Santoro, U. Wegmüller, and B. Rommen. Estimating total aboveground, stem and branch biomass using multi-frequency SAR. *IEEE MultiTemp International Workshop*, 115:1–3, 2017. 15

[19] J. O. Hagberg, L. M. Ulander, and J. I. H. Askne. Repeat-pass SAR interferometry over forested terrain. *IEEE Transactions on Geoscience and Remote Sensing*, 33(2):331–340, 1995. 15

[20] M. Martone, F. Sica, C. Gonzalez, J. L. Bueso-Bello, P. Valdo, and P. Rizzoli. High-Resolution Forest Mapping from TanDEM-X Interferometric Data Exploiting Nonlocal Filtering. *Remote Sensing*, 10:1477, Sep. 2018. 15

[21] M. Martone, P. Rizzoli, C. Wecklich, C. Gonzalez, J. L. Bueso-Bello, P. Valdo, D. Schulze, M. Zink, G. Krieger, and A. Moreira. The Global Forest/Non-Forest Map from TanDEM-X Interferometric SAR Data. *Remote Sensing of Environment*, 205:352–373, Feb. 2018. 15

[22] N. Ackermann, C. Thiel, M. Borgeaud, and C. Schmullius. Cosmo-SkyMed backscatter intensity and interferometric coherence signatures over Germany's low mountain range forested areas. *IGARSS 2012 - 2012 IEEE International Geoscience and Remote Sensing Symposium*, pages 5514–5517, Jul. 2012. 15

[23] J. I. H. Askne, P. B. G. Dammert, L. M. H. Ulander, , and G. Smith. C-Band Repeat-Pass Interferometric SAR Observations of the Forest. *IEEE Transactions on Geoscience and Remote Sensing*, 35(1):25–35, Jan. 1997. 15

[24] F. Mattia, T. Le Toan, G. Picard, F. I. Posa, A. D'Alessio, C. Notarnicola, A. M. Gatti, M. Rinaldi, G. Satalino, and G. Pasquariello. Multitemporal C-band radar measurements on wheat fields. *IEEE Transactions on Geoscience and Remote Sensing*, 41(7):1551–1560, 2003. 15

[25] M. Santoro, J. I. H. Askne, U. Wegmuller, and C. L. Werner. Observations, Modeling, and Applications of ERS-ENVISAT Coherence Over Land Surfaces. *IEEE Transactions on Geoscience and Remote Sensing*, 45(8):2600–2611, 2007. 15

[26] M. E. Engdahl, M. Borgeaud, and M. Rast. The use of ERS-1/2 Tandem interferometric coherence in the estimation of agricultural crop heights. *IEEE Transactions on Geoscience and Remote Sensing*, 39(8):1799–1806, 2001. 15

[27] M. E. Engdahl and J. M. Hyyppa. Land-cover classification using multitemporal ERS-1/2 InSAR data. *IEEE Transactions on Geoscience and Remote Sensing*, 41(7):1620–1628, 2003. 15

[28] T. Strozzi, P. Dammert, U. Wegmüller, J.-M. Martinez, J. I. H. Askne, A. Beaudoin, and N. T. Hallikainen. Landuse mapping with ERS SAR interferometry. *IEEE Transactions on Geoscience and Remote Sensing*, 38(2):766–775, Mar. 2000. 15

[29] A. A. Okhimamhe. ERS SAR interferometry for land cover mapping in a savanna area in Africa. *International Journal of Remote Sensing*, 120(24):3583–3594, May 2010. 15

[30] L. Bruzzone, M. Marconcini, U. Wertmuller, and A. Wiesmann. An Advanced System for the Automatic Classification of Multitemporal SAR Images. *IEEE Transactions on Geoscience and Remote Sensing*, 42(6):1321–1334, Jun. 2004. 15

[31] K. Chureesampant and J. Susaki. Land cover classification using multi-temporal SAR data and optical data fusion with adaptive training sample selection. In *2012 IEEE International Geoscience and Remote Sensing Symposium*, pages 6177–6180, July 2012. 15

[32] D. Geudtner, R. Torres, P. Snoeij, A. Ostergaard, I. Navas-Traver, B. Rommen, and M. Brown. Sentinel-1 system overview and performance. *Living Planet Symposium*, 2013. 15, 18

[33] R. M. Goldstein and H. A. Zebker. Interferometric radar measurement of ocean surface currents. *Nature*, 328(6132):707–709, 1987. 16

[34] R. Touzi, A. Lopes, J. Bruniquel, and P. W. Vachon. Coherence estimation for SAR imagery. *IEEE Transactions on Geoscience and Remote Sensing*, 37(1):135–149, 1999. 16, 23

[35] F. Gatelli, A. M. Guamieri, F. Parizzi, P. Pasquali, C. Prati, and F. Rocca. The wavenumber shift in SAR interferometry. *IEEE Transactions on Geoscience and Remote Sensing*, 32(4), 1994. 16, 22

[36] H. A. Zebker and J. Villasenor. Decorrelation in interferometric radar echoes. *IEEE Transactions on Geoscience and Remote Sensing*, 30(5):950–959, 1992. 16

[37] R. Torres, P. Snoeij, D. Geudtner, D. Bibby, M. Davidson, E. Attema, and F. Rostan. GMES Sentinel-1 mission. *Remote Sensing of Environment*, 120:9–24, 2012. 17

[38] R. Piantanida, N. Miranda, N. Franceschi, and P. Meadows. Thermal Denoising of Products Generated by the S-1 IPF. Technical Report MPC-0392, European Space Agency (ESA), Nov. 2017. 17

[39] G. Krieger, A. Moreira, H. Fiedler, I. Hajnsek, M. Werner, M. Younis, and M. Zink. TanDEM-X: A satellite formation for high-resolution SAR interferometry. *IEEE Transactions on Geoscience and Remote Sensing*, 45(11), 2007. 17, 18

[40] E. Attema, C. Cafforio, M. Gottwald, P. Guccione, A. M. Guarnieri, F. Rocca, and P. Snoeij. Flexible dynamic block adaptive quantization for Sentinel-1 SAR missions. *IEEE Geoscience and Remote Sensing Letters*, 7(4):766–770, 2010. 17

[41] D. Giudici. GMES Sentinel-1 SAR Performance Analysis. Technical Report S1.TN-ARE-PL-0001 version 1.7, European Space Agency, Mar. 2013. 18

[42] A. Moccia and G. Rufino. Spaceborne along-track SAR interferometry: Performance analysis and mission scenarios. *IEEE Transactions on Aerospace and Electronic systems*, 37(1):199–213, 2001. 18

[43] M. Martone, P. Rizzoli, and G. Krieger. Volume decorrelation effects in TanDEM-X interferometric SAR data. *IEEE Geoscience and Remote Sensing Letters*, 13(12):1812–1816, 2016. 18, 19

[44] F. Sica, S. Bretzke, A. Pulella, J. L. Bueso-Bello, M. Martone P. Prats-Iraola, M. J. González-Bonilla, M. Schmitt, and P. Rizzoli. InSAR decorrelation at X-band from the joint TanDEM-X/PAZ constellation. *IEEE Geoscience and Remote Sensing Letters*, 2020. 19

[45] F. Rocca. Modeling interferogram stacks. *IEEE Transactions on Geoscience and Remote Sensing*, 45(10):3289–3299, 2007. 19, 21

[46] F. Sica, A. Pulella, M. Nannini, M. Pinheiro, and P. Rizzoli. Repeat-pass SAR interferometry for land cover classification: A methodology using Sentinel-1 Short-Time-Series. *Remote Sensing of Environment*, pages 111–277, 2019. 20, 26, 27, 36, 43

[47] A. Parizzi, X. Y. Cong, and M. Eineder. First Results from Multifrequency Interferometry. A Comparison of Different Decorrelation Time Constants at L, C and X Band. *ESA Special Publication*, 677, 2010. 21

[48] N. Yague-Martinez, P. Prats-Iraola, F. R. Gonzalez, R. Brcic, R. Shau, D. Geudtner, M. Eineder, and R. Bamler. Interferometric processing of Sentinel-1 TOPS data. *IEEE Transactions on Geoscience and Remote Sensing*, 54(4):2220–2234, 2016. 21

[49] P. Prats, M. Rodriguez-Cassola, L. Marotti, M. Nannini, S. Wollstadt, D. Schulze, N. Tous-Ramon, M. Younis, G. Krieger, and A. Reigber. TAXI: A versatile processing chain for experimental TanDEM-X product evaluation. *IEEE International Geoscience and Remote Sensing Symposium*, pages 4059–4062, Jul. 2010. 22

[50] D. Small. Flattening gamma: Radiometric terrain correction for SAR imagery. *IEEE Transactions on Geoscience and Remote Sensing*, 49(8), 2011. 22

[51] R. K. Raney, A. Freeman, R. W. Hawkins, and R. Bamler. A plea for radar brightness. *International Geoscience and Remote Sensing Symposium*, 2:1090–1090, 1994. 22

[52] L. Breiman. Random forests. *Machine Learning*, 45(1):5–32, Oct. 2001. 23

[53] M. Belgiu and L. Dragut. Random forest in remote sensing: A review of applications and future directions. *ISPRS Journal of Photogrammetry and Remote Sensing*, 114:24–31, 2016. 23

[54] V. F. Rodriguez-Galiano, B. Ghimire, J. Rogan, M. Chica-Olmo, and J. P. Rigol-Sanchez. An assessment of the effectiveness of a random forest classifier for land-cover classification. *ISPRS Journal of Photogrammetry and Remote Sensing*, 67:93–104, 2012. 23

[55] N. Horning. Random Forests: An algorithm for image classification and generation of continuous fields data sets. *In Proceedings of the International Conference on Geoinformatics for Spatial Infrastructure Development in Earth and Allied Sciences*, 911, Dec. 2010. 23

[56] A. D. Kulkarni and B. Lowe. Random forest algorithm for land cover classification. *International Journal on Recent and Innovation Trends in Computing and Communication*, 4(3):58–63, 2016. 23

[57] B. Waskeand and M. Braun. Classifier ensembles for land cover mapping using multitemporal SAR imagery. *ISPRS Journal of Photogrammetry and Remote Sensing*, 64(5):450–457, 2009. 23

[58] L. Breiman, J. H. Friedman, R. A. Olshen, and C. J. Stone. *Classification and regression trees.* Chapman and Hall, 1984. 24

[59] F. Sica P. Posovszky A. Pulella, R. Aragão Santos and P. Rizzoli. Multi-Temporal Sentinel-1 Backscatter and Coherence for Rainforest Mapping. *Remote Sensing*, 12(5):847, 2020. 25, 41

[60] M. A. Unser. Sum and difference histograms for texture classification. *IEEE transactions on pattern analysis and machine intelligence*, 1:118–125, 1986. 25, 26

[61] R. M. Haralick, K. Shanmugam, and I. H. Dinstein. Textural features for image classification. *IEEE Transactions on systems, man, and cybernetics*, 6:610–621, 1973. 25, 26

[62] R. M. Haralick. Statistical and structural approaches to texture. *Proceedings of the IEEE*, 67:786–804, 1979. 25

[63] A. Pulella, F. Sica, and P. Rizzoli. Monthly Deforestation Monitoring with Sentinel-1 Multi-temporal Signatures and InSAR Coherences. *Revista de Teledetección*, 56:1–22, 2020. 28, 41, 52

[64] J. L. Bueso-Bello, P. Rizzoli, M. Martone, and C. González. Potentials of Tandem-X Forest/Non-Forest Map for Change Detection. *IGARSS 2018 - 2018 IEEE International Geoscience and Remote Sensing Symposium*, pages 4213–4216, 2018. 28

[65] S. Beucher. The morphological approach to segmentation: the watershed transform. *Mathematical Morphology in Image Processing*, 1993. 29

[66] M. Drusch, U. Del Bello, S. Carlier, O. Colin, V. Fernandez, F. Gascon, B. Hoersch, C. Isola, P. Laberinti, P. Martimort, A. Meygret, F. Spoto, O. Sy, F. Marchese, and P. Bargellini. Sentinel-2: ESA's Optical High-Resolution Mission for GMES Operational Services. *Remote Sensing of Environment*, 120:25–36, May 2012. 30

[67] M. Main-Knorn, B. Pflug, J. Louis, V. Debaecker, U. Müller-Wilm, and F. Gascon. Sen2Cor for Sentinel-2. In *Image and Signal Processing for Remote Sensing XXIII*, volume 10427, pages 37–48. International Society for Optics and Photonics, SPIE, Oct. 2017. 30

[68] A. Mazza, F. Sica, P. Rizzoli, and G. Scarpa. TanDEM-X forest mapping using convolutional neural networks. *Remote Sensing*, 11(24):2980, 2019. 33

[69] G. Jaffrain and C. Sannier. CORINE Land Cover 2012 Final Validation Report. Technical Report GIO_CLC2012_Validation_Report_SC2_1_4, European Environment Agency, Feb. 2017. 36

[70] D. M. Valeriano, E. M. Mello, J. C. Moreira, Y. E. Shimabukuro, V. Duarte, I. M. I. M. Souza, J. R. dos Santos, C. C. F. Barbosa, and R. C. M. de Souza. Monitoring tropical forest from space: the PRODES digital project. *International Archives of Photogrammetry Remote Sensing and Spatial Information Sciences*, 35:272–274, 2004. 41

[71] M. Kalamandeen, M. Gloor, E. Mitchard, D. Quincey, G. Ziv, D. Spracklen, B. Spracklen, M. Adami, L. Aragão, and D. Galbraith. Pervasive Rise of Small-scale Deforestation in Amazonia. *Scientific Reports*, 8, Dec. 2018. 41